IEEE Transactions on Robotics (T-RO) paper presented at
2024 IEEE/RSJ International Conference on Intelligent Robots and Systems (IROS)
October 14-18, 2024. Abu Dhabi, UAE

Development of Bioinspired Multimodal Underwater Robot "HERO-BLUE" for Walking, Swimming, and Crawling

Taesik Kim, Juhwan Kim, and Son-Cheol Yu, *Member, IEEE*

***Abstract*—This study proposes a novel hybrid underwater robot platform, Hazardous and Extreme environment RObot for Biomimetic multilocomotion-based Underwater Expedition (HERO-BLUE) that integrates swimming and legged motions. HERO-BLUE is equipped with a multimodal fin comprising numerous passive joints that can act as both a swimming fin and a walking limb. This multimodal fin is integrated with a salamander-like spine and soft undulating fin in a single robot system to enable three representative locomotion modes: swimming, walking, and crawling. This article provides details of the hardware configuration of HERO-BLUE, mathematical models for each locomotion mode, motion planning methodology, and control strategies for enabling hybrid motions. For legged motions, a dynamic simulation study was conducted to analyze the ground reaction force. The results verified the effectiveness of the proposed multimodal fin. In water tank experiments, the swimming capability was validated through thrust tests and swimming trials, and the legged motion capability was quantitatively validated in three environments, including gravel, water flow, and slopes. Furthermore, field trials were conducted in real-life scenarios in open seas, lakes, and stream beds. The experimental results show that HERO-BLUE can successively combine swimming and legged motion capability and increase underwater mobility in various challenging underwater environments.**

***Index Terms*—Field robotics, hybrid locomotion, legged robot, marine robotics, multimodal fin, underwater mobility.**

I. Introduction

THE ocean has developed into an enormous food warehouse for humans, a convenient channel for transportation, and a vast power plant; hence, it has great potential in modern society [1], [2], [3]. Underwater robots represented by remotely operated vehicles (ROVs) and autonomous underwater vehicles (AUVs) are considered indispensable scientific equipment for enabling advanced exploration in extreme conditions for humans [4], [5], [6]. Axial thruster-driven locomotion is a conventional method for most ROVs and AUVs to enable hovering or gliding mobility depending on their hardware configurations. AUVs and ROVs contribute to scientific data acquisition [7], [8], [9], underwater structure maintenance [10], [11], nuclear power plant inspection [12], [13], and archeological site exploration [14]. However, despite the numerous robotic applications in various industries, environments comprising torrential streams and swirls or interaction with seabed or aquatic organisms remain a challenge for most thruster-driven ROVs/AUVs.

As the underwater robotics field advances, specific robots categorized as biomimetic underwater robots (BURs) have gained considerable attention.

The fusion of underwater robots and biomimetics is an attractive method for overcoming the intrinsic limitations of thrust-driven underwater robots [15], such as entanglement with seaweed and ecological-footprints in real-life environments [16], [17], [18], [19]. By implementing unique motions based on behavioral and morphological analyses, BURs exhibit improved mobility and efficiency in motion, similar to target organisms, such as snakes [20], [21], [22], octopuses [23], [24], [25], and fishes [26], [27], [28].

Multimodality locomotion is gaining attention as missions are extended to real-life scenarios. The multimodal capability of a robot broadens its potential application owing to high-environmental adaptability and locomotion versatility [29], [30]. Field missions in underwater-related industries, such as maintenance of underwater structures or exploration of sunken ships, can encounter a range of environmental obstacles, including areas covered with seaweed, strong water currents, and confined spaces. To overcome these challenges, a multimodal approach that integrates underwater legged movement and swimming is an appealing hybrid motion strategy. During missions, underwater legged motions can help a robot overcome obstacles, such as shallow water, disturbance of current, and narrow spaces with complex structures. By employing landing and station-keeping functionalities, underwater legged motion can contribute to prolonged and precise examination [18], [31]. Conversely, swimming allows a robot to move faster and more effectively than

Manuscript received 11 May 2023; revised 19 September 2023 and 8 December 2023; accepted 16 December 2023. Date of publication 11 January 2024; date of current version 29 January 2024. This paper was recommended for publication by Associate Editor C. Sung and Editor M. Yim upon evaluation of the reviewers' comments. This work was supported by HERO Lab internal project and the KHNP (Korea hydro and nuclear power company). *(Corresponding author: Son-Cheol Yu.)*

Taesik Kim is with the Department of Convergence IT Engineering, Pohang University of Science and Technology, Pohang 37673, South Korea (e-mail: weed3450@postech.ac.kr).

Juhwan Kim is with the Robot Center, Samsung Research, Samsung Electronics, Seoul 06765, South Korea (e-mail: jurobot.kim@samsung.com).

Son-Cheol Yu is with the Division of Advanced Nuclear Engineering, Pohang University of Science and Technology, Pohang 37673, South Korea (e-mail: sncyu@postech.ac.kr).

This includes four multimedia MPEG-4 format movie clips, which show natural scene of proposed experiments.

This article has supplementary downloadable material available at https://doi.org/10.1109/TRO.2024.3353040, provided by the authors.

Digital Object Identifier 10.1109/TRO.2024.3353040

1941-0468 © 2024 IEEE. Personal use is permitted, but republication/redistribution requires IEEE permission.
See https://www.ieee.org/publications/rights/index.html for more information.

Copyright ©2024 IEEE

Authorized licensed use limited to: POSTECH Library. Downloaded on August 30,2024 at 11:15:24 UTC from IEEE Xplore. Restrictions apply.

legged locomotion, which entails slow travel when overcoming obstacles on the seabed. Several underwater robot platforms have been designed to integrate both legged and swimming motions. Based on the hexapod walking robot platform RHex [32], AQUA [33] with ninja legs [34], and AmphiHex [35], [36], [37] added swimming capability through design and functionality changes in one-degree-of-freedom (DoF) legs. However, they were developed for on-ground walking and, hence, can be greatly affected by drag generated during benthic walking. SHALBOT [38] reduces the drag force generated by the rotational motion and enhances swimming ability and, hence, can be applied in various real-world environments. Nevertheless, entanglement with obstacles, such as ropes and seaweed remains a challenge due to the utilization of rotational legged motion.

Other platforms classified as underwater legged robots [18], [39], [40] have been developed based on morphological features of benthic animals. Equipped with high-DoF limbs and advanced control strategies [41], these robots can achieve precise and sophisticated walking behavior. However, their high-DoF limbs, comprising multiple servos and the links connecting them, increase the demand for electrical power and underwater drag during leg movements. Consequently, these robots encounter difficulties in performing swimming or maneuvering functions other than underwater legged motions, resulting in a high cost of transportation (CoT).

Therefore, this study proposes a novel bioinspired underwater robot platform that is capable of both swimming and legged locomotion in various underwater environments. The Hazardous and Extreme environment RObot for Biomimetic multilocomotion-based Underwater Expedition (HERO-BLUE), simply called BLUE, is a bioinspired robot developed to achieve the following four maneuvering requirements:

1) traverse rough benthic terrain;
2) move on slippery substrate amidst currents;
3) swim in multi-DoF;
4) change modes without requiring hardware replacement/modification during missions.

To incorporate both swimming and legged motions while reducing the number of actuating motors and control complexity, BLUE utilizes a multimodal paddle comprising numerous passive joints driven by a single DoF servo. Consequently, BLUE achieves a precise balance between functionality and efficiency. Furthermore, by integrating specialized biological systems, such as a salamander-like spine mechanism and soft undulating fin with a motion control scheme, BLUE can achieve swimming, walking, and crawling motions to meet the aforementioned maneuvering requirements. The indoor and field experiments indicate that BLUE's multimodality can serve various real-world underwater robotic applications effectively, especially in scenarios with nonflat terrains or water currents, as seen in cave or shipwreck explorations and investigations within confined spaces or underwater structures.

The rest of this article is organized as follows. Section II describes the detailed hardware configurations of the proposed robot, BLUE, and describes the four core modules of BLUE. Section III presents a kinetic model of the robot system and dynamic models for each locomotion mode. In Section IV, the hierarchical control framework is described with a motion generator and three subcontrollers. Section V presents the multibody dynamic simulation results to verify the proposed mathematical models of BLUE, and the proposed legged gaits using the multimodal fins are analyzed. In Section VI, the results of water tank experiments in four environments are presented to verify the mathematical model and evaluate the hybrid mobility of BLUE. Section VII describes the field tests in challenging environments used to evaluate the robustness of the proposed platform. Section VIII discusses the results. Finally, Section IX concludes this article.

TABLE I
MOTION STRATEGIES AND FUNCTIONS OF CORE ELEMENTS

Mode	Pec. fin	Lat. fin	Spine	Buoy
Walking	Limb	-	*Rot.	Negative (high)
Crawling	Limb	-	Undul. *Rot.	Negative (high)
Slope walking	Limb	Down-force	*Rot.	Negative (low)
Swimming	Fin $(x^{\mathrm{P}},z^{\mathrm{P}})$	Fin $(x^{\mathrm{L}},y^{\mathrm{L}},z^{\mathrm{L}})$	*Rot.	Neutral

* This motion is not covered in this paper article.

II. SYSTEM DESIGN

BLUE is 0.6 m wide, 0.3 m tall, and 0.8 m long, and it has a mass of 11.32 kg. As shown in Fig. 1, the hardware components of BLUE are divided into two main parts: the front body, which includes various sensors (two eye camera modules, an inertial navigation system, and a pressure sensor) and built-in computing units, and the rear body, which includes a battery and power management modules. BLUE comprises eleven servos, nine of which are exposed to the outside of the body to create swimming or legged motions, whereas the remaining two control buoyancy within the body. The nine external servos are responsible for actuating four pectoral fins, two lateral fins, and a spine joint that connects the front and rear bodies. To achieve multimodal locomotion without hardware exchanges during missions, BLUE employs four core elements: pectoral fins, lateral fins, spine system, and active buoyancy controllers (ABCs). The pectoral and lateral fins serve as the primary actuators of BLUE. The pectoral fins allow BLUE to perform hybrid underwater locomotion by performing the roles of both limbs and swimming fins. The lateral fins increase the DoFs and walking stability in swimming and slope walking modes, respectively. The spine system enables rotation in the yaw direction of the torso and can create a crawling gait with the pectoral fins. The ABCs located in front of each body cylinder adjust the buoyancy to increase the electrical efficiency according to the locomotion mode. Fig. 2 schematically illustrates BLUE's locomotion mode to the target environment, whereas Table I summarizes the functions of each core element with respect to the target movements. The subsequent sections elaborate on the core elements' features, structure, and principles, followed by a detailed description of the proposed robot's electrical architecture and its components.

Authorized licensed use limited to: POSTECH Library. Downloaded on August 30,2024 at 11:15:24 UTC from IEEE Xplore. Restrictions apply.

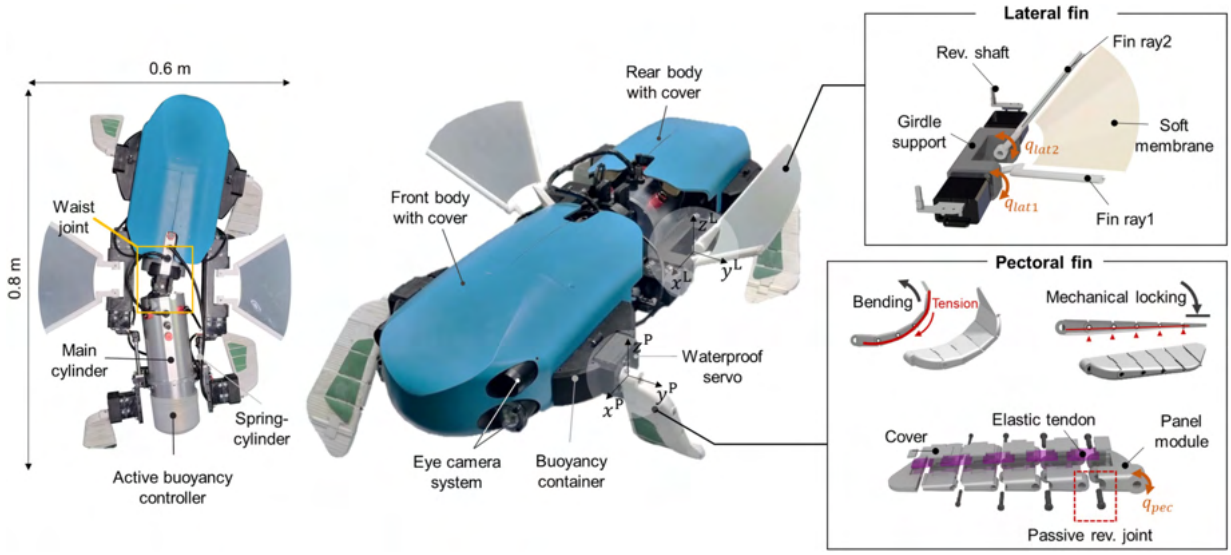

Fig. 1. Underwater hybrid robot BLUE: Hardware configuration and main components.

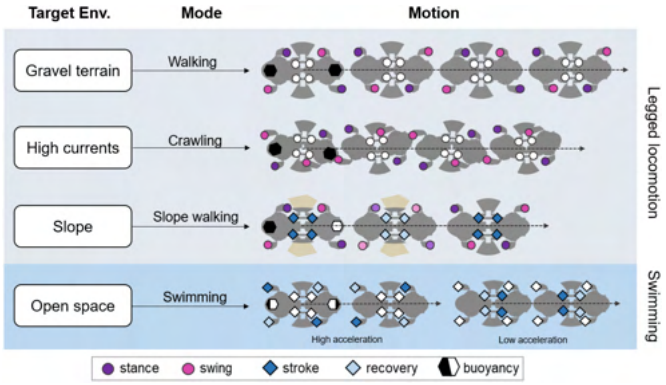

Fig. 2. Target environment and proposed locomotion modes of BLUE. In the hexagonal symbol, black indicates low buoyancy, and white indicates high buoyancy.

A. Bioinspired Fins

1) Pectoral Fins With Passive Locking Mechanism: The four pectoral fins, which are symmetrically located at each corner of the robot body, are 8 cm wide, 19 cm long, and 2 cm thick. The pectoral fins have semisoft physical properties, meaning they can be either rigid or soft depending on the direction of rotation during interaction with the aquatic environment or substrate. Each pectoral fin comprises six panel modules that are linked by five revolute joints and artificial tendons made of silicone using custom molds; those placed close to the hip joint have strong elasticity. The artificial elastic tendons are fixed inside the panel and protected by covers to prevent damage, such as scratches or tears. The pectoral fins have passive torque in a clockwise (CW) direction during counterclockwise bending owing to the passive tension of each artificial tendon (see Fig. 1). However, in CW bending at the neutral position, the panels are mechanically locked to ensure they do not rotate in the CW direction. As a result, the pectoral fins exhibit semisoft properties with a multiarticular structure and artificial tendons that bend in only one direction during interaction with water or substrate due to passive tension. Therefore, by controlling the servo connected to each pectoral fin, the pectoral fin can generate thrust using oscillatory motion in the swimming fin mode, which is similar to the methodology used in [42] and [43]. In the leg mode, the anisotropic property of the pectoral fin can effectively alter the frictional force of the substrate according to the stance and swing phases, which is further analyzed in Section V.

2) Lateral Fins With Soft Membrane: Aquatic organisms, such as knife fish, cuttlefish, eels, and stingrays, have evolved to generate thrust by sending traveling waves along their undulating fin [44], [45], which allows them to achieve multidirectional maneuvers with high efficiency at low speeds. Similar to those developed in previous studies [46], [47], the motion of BLUE's lateral fins can generate thrust by mimicking the undulating motion of a ray-fin fish. The lateral fins are symmetrically located on each side of the robot's waist, and each lateral fin is controlled by two waterproof servos located along x^L. By changing the phase differences (φ^{L}) between two servos, the lateral fin can create both oscillating ($\varphi^{\mathrm{L}} = 0$) and undulating ($\varphi^{\mathrm{L}} = 0.5\pi$) motions. The two rays are connected to a 3-mm-thick flexible material (silicone), whose trapezoidal shape increases the contact area with water and is distorted by the angular phase difference between the two actuators. The lateral fins work together with the pectoral fins to implement advanced motions as well as swimming functions.

B. Spine With PRRP Closed-Chain Mechanism

The waist components of BLUE connect the front and rear bodies forming the spine mechanism, and are designed to mimic the crawling gait of a salamander or rock-climbing fish [48], [49], whose unique crawling motion allows efficient movement on slippery surfaces under torrential streams by lowering their body and increasing the contact area between the fin surface

Authorized licensed use limited to: POSTECH Library. Downloaded on August 30,2024 at 11:15:24 UTC from IEEE Xplore. Restrictions apply.

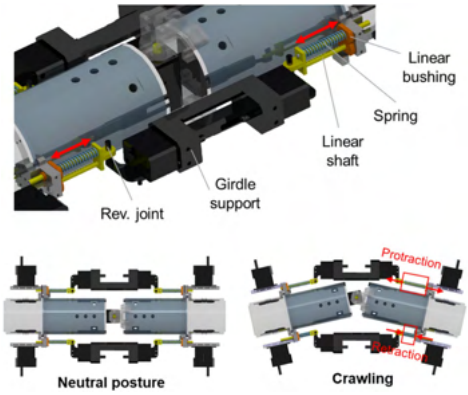

Fig. 3. Components of the spine structure and its movement mechanism.

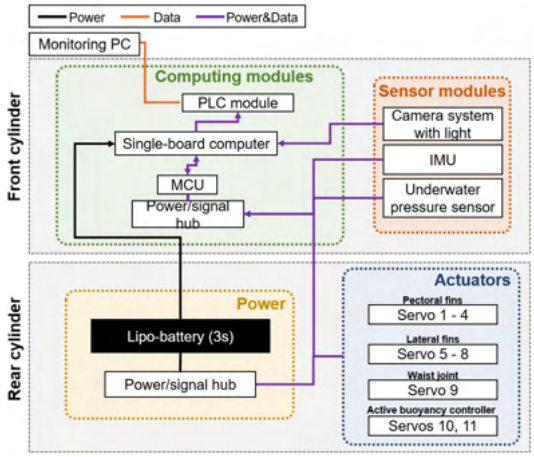

Fig. 4. Electronic architecture of BLUE.

and substrate. To avoid mechanical interference between the bioinspired fins and bodies, the waist joint and girdle support comprise a PRRP (P: prismatic, R: rotational) closed-chain movable linkage, which links a prismatic joint comprising a linear shaft and linear bushing to the girdle support with a revolute joint (see Fig. 3). A spring located at the linear shaft maintains the position of the girder support in the center and extends the maximum rotation range of the waist by contracting and expanding according to the robot's waist movement. Therefore, the waist joint can undulate without mechanical locking between the girdle support and front/rear bodies, thereby enabling a range of rotation of less than 30°.

C. Active Buoyancy Controller

To achieve hybrid locomotion, the optimal magnitude of buoyancy differs according to the locomotion mode of the robot. To swim efficiently, the robot requires neutral buoyancy or slightly high buoyancy (for recovery) to prevent the constraint of the gravitational force. Conversely, to perform effective benthic locomotion, locomotion gaits require negative buoyancy to generate high downforce to prevent slippage between the robot's contact points and substrate. Therefore, two ABCs are attached to the front and rear cylinders of the robot (see Fig. 1). By converting the rotational motion of the servo into the linear motion of the screw, the ABCs can modify its volume and buoyancy. The front buoyancy and rear buoyancy can be controlled in the range of 0–5.88 N. BLUE has a buoyancy modification capability of 1.2 kgf, which is larger than the underwater weight of BLUE (1.1 kgf in freshwater). This indicates that BLUE can switch between negative and positive buoyancy. The detailed dynamic model and control strategy of the ABCs are described in Sections III and IV, respectively.

D. Electronic Components

All electronic components for the robot operation/control are waterproofed by the two main cylinders (front and rear) inside the body cover. As shown in Fig. 4, the front cylinder comprises a single-board computer (Nvidia Jetson-TX2) that runs the robot operating system. The single-board computer communicates with an external monitoring computer via a power-line communication module and is connected to a microcontroller unit (MCU). The MCU (32-bit ARM Cortex-M3 core) receives and processes the linked sensor data at 90-ms intervals and simultaneously controls the 11 servo motors at 15-ms intervals. The front cylinder contains an inertial measurement unit (IMU) and underwater pressure sensors. The IMU with the extended Kalman filter [50] measures the angular rate and multiaxis robot accelerations and estimates the Euler angle of the robot. The rear cylinder contains a power subsystem comprising a battery (LiPo 3S–5200 mAh), which is connected to all electronic components through a power cable and power/signal hub. The front and rear bodies share their communication and power; BLUE can operate stand-alone through a communication line with an external computer. The pectoral and lateral fins are actuated in the water by four servos (Dynamixel XH-430-W350-R) with customized waterproof aluminum shells. The corresponding servo inside the main cylinder operates ABC. The waist joint is activated by a more powerful servo (Dynamixel XH-540-W350-R), considering the mechanical load acting on the joint. All servos are connected via power/signal hubs and controlled simultaneously by the MCU.

III. Mathematical Model and Motion Planning

A. Kinematic Model

The proposed robot system comprises a body consisting of two cylinders, two pairs of pectoral fins, one pair of lateral fins, and two integrated ABCs. Assuming that the body fixed frame $\{B\}$ is located at the center (b) of the robot's waist joint, the two body frames $\{B_1\}$ and $\{B_2\}$ centered at b_1 and b_2, respectively, the pectoral fin frames $\{P_i\}$ centered at p_i, and the lateral fin frames L_i centered at l_i (see Fig. 5). These listed frames and center points have the following kinematic relationships expressed in position vectors $\mathbf{r}$ in $\{B\}$:

$$\mathbf{r}_{bb_1} = [d_b,\, 0,\, 0], \quad \mathbf{r}_{bb_2} = [-d_b c(q_9),\, -d_b s(q_9),\, 0] \tag{1}$$

$$\mathbf{r}_{bp_1} = [d_{px},\, d_{py},\, 0], \quad \mathbf{r}_{bp_2} = [d_{px},\, -d_{py},\, 0] \tag{2}$$

Authorized licensed use limited to: POSTECH Library. Downloaded on August 30,2024 at 11:15:24 UTC from IEEE Xplore. Restrictions apply.

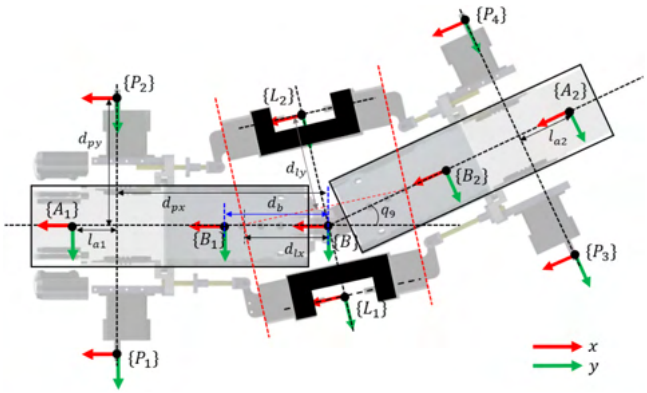

Fig. 5. Kinematic model of BLUE.

$$\mathbf{r}_{bp_3} = [-d_{px}c(q_9) - d_{py}s(q_9),\ -d_{px}s(q_9) + d_{py}c(q_9),\ 0] \tag{3}$$

$$\mathbf{r}_{bp_4} = [-d_{px}c(q_9) + d_{py}s(q_9),\ -d_{px}s(q_9) - d_{py}c(q_9),\ 0] \tag{4}$$

$$\mathbf{r}_{bl_1} = \left[-s(q_9)\left(d_{ly} + d_{lx}s\left(\frac{q_9}{2}\right)\right),\ c(q_9)\left(d_{ly} + d_{lx}s\left(\frac{q_9}{2}\right)\right),\ 0\right] \tag{5}$$

$$\mathbf{r}_{bl_2} = \left[-s(q_9)\left(d_{ly} - d_{lx}s\left(\frac{q_9}{2}\right)\right),\ c(q_9)\left(d_{ly} - d_{lx}s\left(\frac{q_9}{2}\right)\right),\ 0\right] \tag{6}$$

where $s(\cdot)$ and $c(\cdot)$ denote $\sin(\cdot)$ and $\cos(\cdot)$, respectively. For the two ABCs, the center points a_1, a_2, and their frames $\{A_1\}$, $\{A_2\}$ can be expressed in $\{B\}$ as follows:

$$\mathbf{r}_{ba_1} = [d_{px} + l_{a1},\ 0,\ 0] \tag{7}$$

$$\mathbf{r}_{ba_2} = [-(d_{px} + l_{a2})c(q_9),\ -(d_{px} + l_{a2})s(q_9),\ 0] \tag{8}$$

$$\mathbf{r}_{ba_0} = [0,\ 0,\ d_0] \tag{9}$$

B. Dynamic Model

As shown in Fig. 6(a), BLUE changes its method of body traction according to the locomotion mode. To integrate hybrid motion, the dynamic model of BLUE is based on dynamic models for legged robots [51], [52], AUV [53], and BUR [20]. Table II summarizes the specific descriptions of the abbreviations used in the proposed and following dynamic models of BLUE. The proposed dynamic equation of motion regarding the joint configuration illustrated in Fig. 6(b) can be expressed as

$$\begin{aligned}&\mathbf{M}(\mathbf{q})\dot{\mathbf{u}} + \mathbf{C}(\mathbf{u})\mathbf{u} + \mathbf{D}(\mathbf{u})\mathbf{u} + g(\mathbf{q})\\ &\quad = \mathbf{J}_{\text{ext}}^{\text{T}}\mathbf{F}_{\text{ext}} + \mathbf{S}_{\text{a}}\boldsymbol{\tau} + \mathbf{S}_{\text{p}}\boldsymbol{\tau}\end{aligned} \tag{10}$$

where $\mathbf{q}$ and $\mathbf{u}$ denote the generalized coordinates and velocity, respectively, as follows:

$$\mathbf{q} = \begin{bmatrix}\boldsymbol{\eta} & \mathbf{q}_{\text{a}} & \mathbf{q}_{\text{p}}\end{bmatrix}^{\text{T}}, \mathbf{u} = \begin{bmatrix}\mathbf{u}_{\text{B}} & \dot{\mathbf{q}}_{\text{a}} & \dot{\mathbf{q}}_{\text{p}}\end{bmatrix}^{\text{T}}. \tag{11}$$

$\mathbf{q}$ includes six-DoF unactuated base coordinates $\boldsymbol{\eta} = [x_B, y_B, z_B, \phi_B, \theta_B, \psi_B]$, active joint coordinates $\mathbf{q}_a = [q_1, \ldots, q_9]$, and passive joint coordinates $\mathbf{q}_p = [\varepsilon^1{}_1, \ldots, \varepsilon^4{}_5]$. The kinematic relationship between $\boldsymbol{\eta}$ and the linear and angular velocity vector $\mathbf{u}_{\text{B}} = [u, v, w, p, q, r]$ follows Euler angle representation [53], which expresses the relationship using a transformation matrix $\mathbf{J}_{\text{B}}$ as follows: $\dot{\boldsymbol{\eta}} = \mathbf{J}_{\text{B}}(\boldsymbol{\eta})\mathbf{u}_{\text{B}}$. The matrices $\mathbf{M}(\mathbf{q})$, $\mathbf{C}(\mathbf{u})$, and $\mathbf{D}(\mathbf{u})$ represent the multibody inertia matrix, Coriolis and centrifugal matrix, and hydro-dynamic damping matrix, respectively. The vectors $g(\mathbf{q})$, $\mathbf{F}_{\text{ext}}$, and $\boldsymbol{\tau}$ denote the gravitational forces/moments, external forces/moments, and generalized torque input, respectively. The selective matrices, $\mathbf{S}_{\text{a}}$ and $\mathbf{S}_{\text{p}}$, perform the following operations on $\boldsymbol{\tau}$:

$$\mathbf{S}_{\text{a}}\boldsymbol{\tau} = \begin{bmatrix}\mathbf{0} & \boldsymbol{\tau}_{\text{a}} & \mathbf{0}\end{bmatrix}^{\text{T}}, \mathbf{S}_{\text{p}}\boldsymbol{\tau} = \begin{bmatrix}\mathbf{0} & \mathbf{0} & \boldsymbol{\tau}_{\text{p}}\end{bmatrix}^{\text{T}}. \tag{12}$$

The passive joints of the pectoral fin were modeled as a torsional spring damper system, as shown in Fig. 6(c). The corresponding element of $\boldsymbol{\tau}_{\text{p}}$ depends on the implementation of mechanical interlocking between the passive joints

$$\left[\boldsymbol{\tau}_{\text{p}}\right]_j^i = \begin{cases} -k_j(\varepsilon_j^i + \varepsilon_{\text{eq}j}) - c_j\dot{\varepsilon}_j^i & \text{(move)} \\ -k_j(\varepsilon_{\text{eq}j}) - c_j\dot{\varepsilon_j}^i + \left[\boldsymbol{\tau}_{\text{p}}\right]_{j-1}^i & \text{(locked)} \end{cases} \tag{13}$$

$$\left[\boldsymbol{\tau}_{\text{p}}\right]_0^i = \left[\boldsymbol{\tau}_{\text{a}}\right]^i \tag{14}$$

where the superscript i denotes the ith pectoral fin, subscript j denotes the jth passive joint, and k_j, $\varepsilon_{\text{eq}}j$, and c_j have the same values regardless of the number of the pectoral fins.

From the proposed dynamic model (10), the partial dynamic model for unactuated floating base $\{B\}$ can be expressed as

$$\begin{aligned}&[\mathbf{M}(\mathbf{q})\dot{\mathbf{u}}]_B + [\mathbf{C}(\mathbf{u})\mathbf{u}]_B + [\mathbf{D}(\mathbf{u})\mathbf{u}]_B\\ &\quad + [g(\mathbf{q})]_B = [\mathbf{F}_{\text{ext}}]_B.\end{aligned} \tag{15}$$

For the hydrodynamic term $[\mathbf{D}(\mathbf{u})\mathbf{u}]_B$, both linear ($\mathbf{F}^{\text{I}}$) and quadratic ($\mathbf{F}^{\text{II}}$) drag forces are considered, which are expressed in the vector form as follows:

$$[\mathbf{D}(\mathbf{u})\mathbf{u}]_B = [\mathbf{F}_{\text{D}_{\text{b}1}} + \mathbf{F}_{\text{D}_{\text{b}2}}] \in \mathbb{R}^{6\times 1} \tag{16}$$

TABLE II
PARAMETERS FOR DYNAMIC MODEL OF BLUE

Abbreviation	Definition
$\mathbf{q}$	Generalized coordinate
$\mathbf{u}$	Generalized velocity
$\boldsymbol{\tau}$	Generalized torque
$\boldsymbol{\tau}_{\text{a}}$	Active joints torque
$\boldsymbol{\tau}_{\text{p}}$	Passive joints torque
$q_i(\forall i \in \{1...4\})$	Active joints of pectoral fin
$q_i(\forall i \in \{5...8\})$	Active joints of lateral fin
q_9	Active joint of spine
$\varepsilon_i(\forall i \in \{1...5\})$	Angles of passive joints in pectoral fin
$\varepsilon_{\text{eq}i}(\forall i \in \{1...5\})$	Equilibrium angle of ε_i
$k_i(\forall i \in \{1...5\})$	Torque spring coefficient of ε_i
$c_i(\forall i \in \{1...5\})$	Damping coefficient of ε_i
n_c	Maximum number of contact points for each leg
$\mathbf{S}_{\text{a}}, \mathbf{S}_{\text{p}}$	Selective matrices
$\mathbf{J}_{\text{ext}}$	Jacobian matrix toward applying points of $\mathbf{F}_{\text{ext}}$
$\mathbf{F}_{\text{ext}}$	External force vector
$\mathbf{M}(\mathbf{q})$	Multibody mass matrix
$\mathbf{C}(\mathbf{u})$	Coriolis and centrifugal matrix
$\mathbf{D}(\mathbf{u})$	hydrodynamic damping matrix

Authorized licensed use limited to: POSTECH Library. Downloaded on August 30,2024 at 11:15:24 UTC from IEEE Xplore. Restrictions apply.

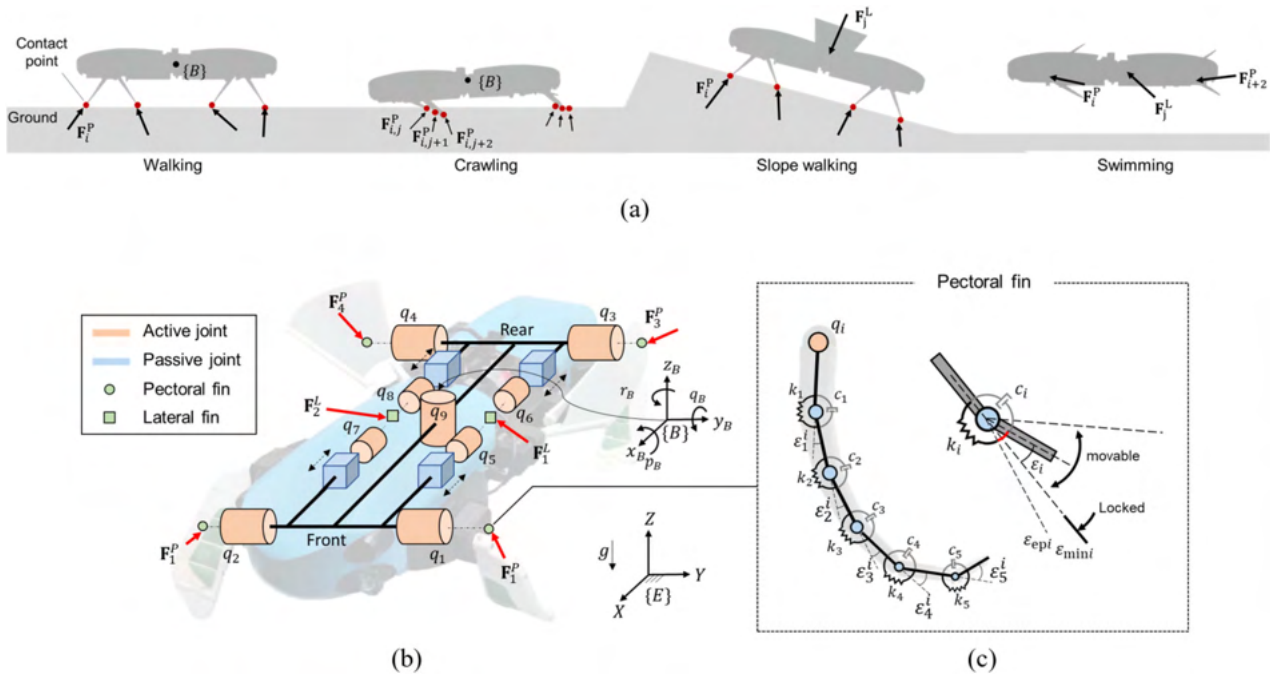

Fig. 6. Dynamic model and joint configuration of BLUE. (a) Body traction method of BLUE according to the locomotion mode. (b) The joint configuration of BLUE's body. (c) The kinematic structure of pectoral fin.

where

$$\mathbf{F}_{\mathrm{D}_{bi}} = [\mathcal{A}_{T_{B_iB}}]^{\mathrm{T}}(\mathbf{F}^{\mathrm{I}}_{D_{bi}} + \mathbf{F}^{\mathrm{II}}_{D_{bi}}) \tag{17}$$

$$\mathbf{F}^{\mathrm{I}}_{D_{bi}} = \mathbf{K}^{\mathrm{I}}_i \mathbf{V}_i, \quad \mathbf{F}^{\mathrm{II}}_{D_{bi}} = \mathbf{K}^{\mathrm{II}}_i \mathbf{sgn}(\mathbf{V}_i)\mathbf{V}_i\mathbf{V}_i^{\mathrm{T}}. \tag{18}$$

The vectors $\mathbf{F}_{\mathrm{D_{b1}}}$ and $\mathbf{F}_{\mathrm{D_{b2}}}$ represent the drag forces acting on b_1 and b_2, respectively, with respect to $\{B\}$. The matrix $[\mathcal{A}_{T_{B_iB}}] \in \mathbb{R}^{6\times6}$ represents the adjoint mapping matrix based on transformation matrix $\mathbf{T}_{B_iB} = (\mathbf{R}_{B_iB}, \mathbf{p}_{B_iB}) \in \mathrm{SE}(3)$. The matrices $\mathbf{K}^{\mathrm{I}}_i$ and $\mathbf{K}^{\mathrm{II}}_i$ are diagonal matrices, which include the linear and quadratic damping coefficient, respectively. The vector $\mathbf{V}_i$ denotes the linear and angular velocity of $\{B_i\}$.

The gravitational force term $[g(\mathbf{q})]_{\mathrm{B}}$ includes both gravity and buoyancy of the body, which involves the operations of the two ABCs. The center of buoyancy (CoB) of the bodies without the ABCs is located at a_0, and the CoB of the front and rear ABC are located at a_1 and a_2, respectively. $[g(\mathbf{q})]_{\mathrm{B}}$ can be expressed in the vector form as follows:

$$[g(\mathbf{q})]_{\mathrm{B}} = \begin{bmatrix} {}^{B}\mathbf{F}_{\mathrm{G}} \\ \mathbf{r}_{bc} \times {}^{B}\mathbf{F}_{\mathrm{G}} \end{bmatrix} + \begin{bmatrix} \sum_{i=0}^{2} {}^{B}\mathbf{F}_{\mathrm{a}_i} \\ \sum_{i=0}^{2} \mathbf{r}_{ba_i} \times {}^{B}\mathbf{F}_{\mathrm{a}_i} \end{bmatrix} \tag{19}$$

where c is the center of gravity and $\mathbf{F}_{\mathrm{G}}$ is the gravitational force vector on c. $\mathbf{F}_{a0}$, $\mathbf{F}_{a1}$, and $\mathbf{F}_{a2}$ are the buoyancy vectors acting on b_1, b_2, and b_3, respectively. Because the moving part of the ABC has a cylindrical structure, we can calculate the buoyancy vectors as ${}^{I}\mathbf{F}_{a_0} = [0, 0, F_{a0}]^T$, ${}^{I}\mathbf{F}_{a_1} = [0, 0, \rho g A \Delta l_{a1}]^T$, and ${}^{I}\mathbf{F}_{a_2} = [0, 0, \rho g A \Delta l_{a2}]^T$. The constants ρ, g, and A denote the density of water, gravity acceleration, and cross-sectional area of the ABC, respectively. The scalar Δl_a is the displacement of the ABC driven by the intrinsic screw motion.

The external force term $[\mathbf{F}_{\mathrm{ext}}]_B$ can be calculated as the summation of external forces and moments acting on $\{B\}$, which comprises the forces generated by pectoral fins ($\mathbf{F}^{\mathrm{P}}_i$) and lateral fins ($\mathbf{F}^{\mathrm{L}}_i$). Note that, unlike the lateral fins, the pectoral fins generate external force using distinct mechanisms depending on the operation mode. In swimming mode, the pectoral fins interact with the water to generate a direct thrust, and $[\mathbf{F}_{\mathrm{ext}}]_B$ can be formulated as follows:

$$[\mathbf{F}_{\mathrm{ext}}]_B = \sum_{i=1}^{2} [\mathcal{A}_{T_{L_iB}}]\mathbf{F}^{\mathrm{L}}_i + \sum_{j=1}^{4} [\mathcal{A}_{T_{BP_j}}]\mathbf{F}^{\mathrm{P}}_j \quad (n_c = 0). \tag{20}$$

In the walking and crawling modes, the pectoral fins generate ground reaction force (GRF) by interacting with the substrate. Depending on the maximum number of contact points (n_c) for each leg, $[\mathbf{F}_{\mathrm{ext}}]_B$ can be expressed as follows:

$$\left[\mathbf{F}_{\mathrm{ext}}\right]_B = \sum_{i=1}^{2} [\mathcal{A}_{T_{L_iB}}]\mathbf{F}^{\mathrm{L}}_i + \sum_{j=1}^{4} [\mathbf{J}^{\mathrm{T}}_{c_j}\mathbf{F}^{\mathrm{P}}_j]_B \quad (n_c = 1) \tag{21}$$

$$\left[\mathbf{F}_{\mathrm{ext}}\right]_B = \sum_{i=1}^{2} [\mathcal{A}_{T_{L_iB}}]\mathbf{F}^{\mathrm{L}}_i + \sum_{j=1}^{4}\sum_{k=1}^{n_c} [\mathbf{J}^{\mathrm{T}}_{c_{j,k}}\mathbf{F}^{\mathrm{P}}_{j,k}]_B \quad (n_c > 1). \tag{22}$$

Here, the total GRF vector ($\mathbf{F}_{\mathrm{gr}}$) can be calculated as the sum of the pectoral fin forces during stance ($\mathbf{F}^{\mathrm{st}}_{\mathrm{gr}}$) and swing ($\mathbf{F}^{\mathrm{sw}}_{\mathrm{gr}}$) states, expressed as follows:

$$\mathbf{F}_{\mathrm{gr}} = \mathbf{F}^{\mathrm{st}}_{\mathrm{gr}} + \mathbf{F}^{\mathrm{sw}}_{\mathrm{gr}} = [\mathbf{F}_{\mathrm{ext}}]_B - \sum_{i=1}^{2} [\mathcal{A}_{T_{BL_i}}]\mathbf{F}^{\mathrm{L}}_i. \tag{23}$$

Authorized licensed use limited to: POSTECH Library. Downloaded on August 30,2024 at 11:15:24 UTC from IEEE Xplore. Restrictions apply.

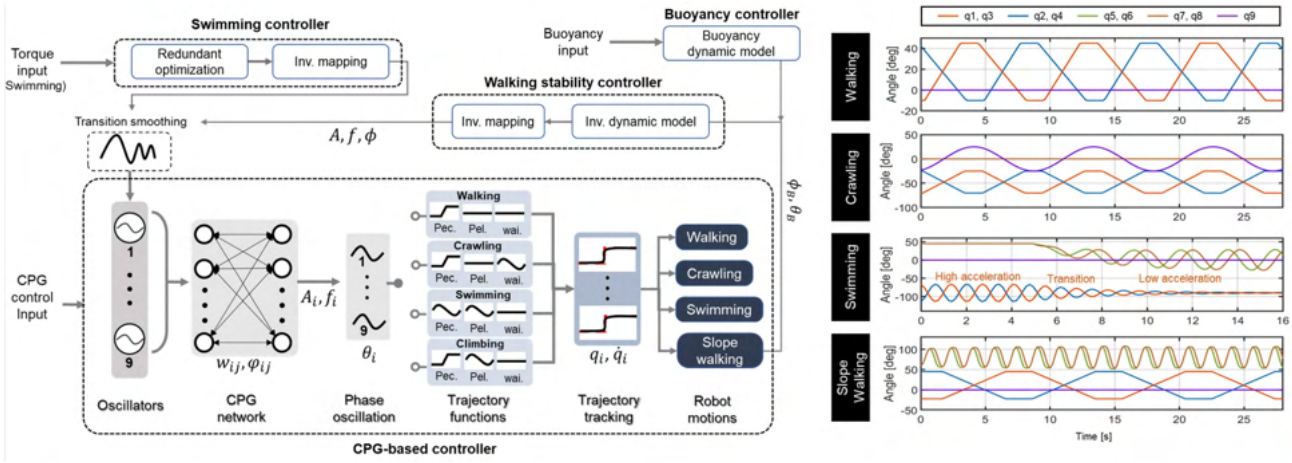

Fig. 7. Schematic diagram of hybrid motion control and generated joint trajectories.

IV. Control Strategies

Fig. 7 shows the hierarchical motion control architecture for managing the versatile locomotion of BLUE. The central pattern generator (CPG)-based trajectory generator is the main control layer in the proposed control architecture, and three subcontrollers are applied depending on the mode.

The swimming controller is a feedforward controller that achieves the desired torque distribution by inverse mapping through redundant optimization and trajectory pattern generation based on proposed motion planning. The walking stability controller is a model-based feedback controller that controls the lateral fins to satisfy a nonslip condition required for stable walking on a slope. The buoyancy controller is a model-based controller that enables hybrid mode switching and pitch angle control to optimize body posture on slopes with varying inclinations.

A. Motion Pattern Generation

In nature, CPGs, the fundamental network of neurons, generate and transmit a rhythmic electrical signal, which allows the muscles to perform rhythmic movements. With mathematical models of various nonlinear oscillators [54], CPG control is an effective approach for creating various periodic motions in biomimetic robotics that required to move in a delicate gait [55] and multimode [30], [56], [57]. We developed customized CPG networks to generate different types of rhythmic patterns to coordinate organic movements between the waist, lateral fins, and pectoral fins to implement target locomotion. The proposed CPG model was constructed with nine oscillators assigned to each servo to generate time trajectories of the nine servos in charge of the biomimetic fins and waist. The Kuramoto model [58] was applied as a nonlinear oscillator because it can manage a large set of coupled oscillators

$$\dot{\theta}_i = 2\pi f_i + \sum_j r_i w_{ij} \sin(\theta_j - \theta_i - \varphi_{ij}) \tag{24}$$

$$\theta_i = \theta_i \bmod 2\pi \tag{25}$$

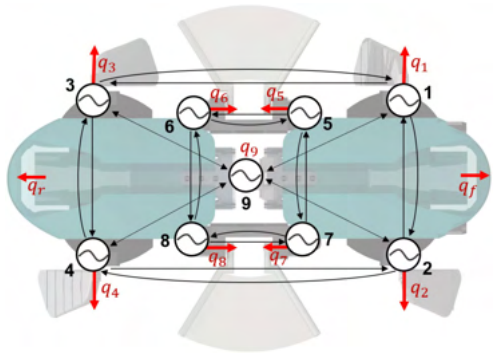

Fig. 8. CPG oscillator configuration and topology of proposed CPG networks.

where θ_i and f_i represent the phase and frequency of ith oscillator, respectively; r_i denotes the intrinsic amplitude; and w_{ij} and φ_{ij} are the weight term and phase offset, respectively. The assigned CPG oscillators are functionally grouped into the pectoral CPG group (#1–4), lateral CPG group (#5–8), and waist CPG (#9). Fig. 8 shows the topology and connections of the proposed CPG network. The mathematical correlation of the CPG networks can be represented by the weight matrix ($\mathbf{W}$) and the offset matrix ($\mathbf{P}$), which are symmetric and skew-symmetric, respectively

$$\mathbf{W} = \begin{bmatrix} w_{11} & \cdots & w_{19} \\ \vdots & \ddots & \vdots \\ w_{19} & \cdots & w_{99} \end{bmatrix}, \mathbf{P} = \begin{bmatrix} \varphi_{11} & \cdots & \varphi_{19} \\ \vdots & \ddots & \vdots \\ -\varphi_{19} & \cdots & \varphi_{99} \end{bmatrix}. \tag{26}$$

The constant matrix $\mathbf{W}$ numerically expresses the degree of coupling between the CPG oscillation models, and matrix $\mathbf{P}$ represents the phase difference between the CPG oscillation models. Although the categorized CPG groups are structurally fully connected, each group can act independently depending on the elements of $\mathbf{W}$. In this study, the pectoral CPG group and waist CPG are integrated to create organic movements, such as crawling and swimming. The lateral CPG group acts independently to increase the control redundancy during swimming

Authorized licensed use limited to: POSTECH Library. Downloaded on August 30,2024 at 11:15:24 UTC from IEEE Xplore. Restrictions apply.

and walking on a slope. The elements of $\mathbf{P}$ for the pectoral fins maintain constant values to implement the quadruped diagonal gait, and the lateral/waist CPG groups are controlled depending on the swimming motions (lateral fin undulating and oscillating) and locomotion modes (crawling and swimming), respectively.

Each phase (θ_i) is determined through the CPG network and converted into an instantaneous target position (q_i) at the servo level using multiple predefined trajectory functions. The trajectory functions are expressed as a different mathematical function in terms of θ_i depending on the robot mode

$$q_i = \begin{cases} \Psi_i^P + A_i^P \cos(\theta_i) & 1 \le i \le 4\,(\text{swim}) \\ f(\theta_i) & 1 \le i \le 4\,(\text{walk/crawl}) \\ \Psi_i^L + A_i^L \cos(\theta_i) & 5 \le i \le 9 \end{cases} \tag{27}$$

and with a convergence smoothing controller

$$\dot{\psi}_i = \alpha(\Psi_i - \psi_i) \tag{28}$$

$$\dot{a}_i = \beta(A_i - a_i) \tag{29}$$

where Ψ_i and A_i represent the target offset angle and amplitude and ψ_i and a_i represent the instantaneous offset angle and amplitude, respectively. The indices P and L denote the pectoral and lateral fins, respectively. Constants α and β denote smoothing control gains. The trajectory function $f(\theta_i)$ mapping between θ_i and q_i is modified as follows according to the order of intervals ($\theta_i = [0, \lambda_{\rm d}), [\lambda_{\rm d}, \lambda_{\rm d} + \lambda_{\rm st}), [\lambda_{\rm d} + \lambda_{\rm st}, 3\lambda_{\rm d} + \lambda_{\rm st}), [3\lambda_{\rm d} + \lambda_{\rm st}, 3\lambda_{\rm d} + \lambda_{\rm st} + \lambda_{\rm sw}), [3\lambda_{\rm d} + \lambda_{\rm st} + \lambda_{\rm sw}, 2\pi)$) as

$$f(\theta_i) = \begin{cases} q_{\max} \\ (\theta_i - \lambda_{\rm d})(q_{\min} - q_{\max})/\lambda_{\rm st} + q_{\max} \\ q_{\min} \\ (\theta_i - 3\lambda_{\rm d} - \lambda_{\rm st})(q_{\max} - q_{\min})/\lambda_{\rm sw} + q_{\min} \\ q_{\max} \end{cases} \tag{30}$$

$$\lambda_{\rm d} = \pi - \frac{(\lambda_{\rm st} + \lambda_{\rm sw})}{2} \tag{31}$$

where $q_{\max}$ and $q_{\min}$ denote the maximum and minimum angles and $\lambda_{\rm st}$ and $\lambda_{\rm sw}$ are the phase lengths of the stance and swing phase, respectively.

B. Inverse CPG Mapping

The direction and magnitude of the thrust of the pectoral and lateral fins were correlated with several CPG input variables. Using the amplitude (A), offset angle (Ψ), frequency (f), and phase shift (φ), the thrust vectors of the pectoral and lateral fins can be expressed as the following multivariable mapping function: $\mathbf{f}_{\rm pec} = \mathbf{M}_{\rm pec}(A, f, \Psi)$ and $\mathbf{f}_{\rm lat} = \mathbf{M}_{\rm lat}(A, f, \varphi^{\rm L}, \Psi)$. To increase the linearity of the two mapping functions and simplify the inverse mapping process, the frequency and $\psi_{\rm L}$ were set as constants in switchable form. Based on the data acquired in the thrust experiments (see Section V), the inverse mapping function was determined through the linear regression method closely following [42], [59].

C. Walking Stability Controller on a Slope

During walking gait, the GRF acting on the pectoral fin exhibits diverse mechanical stiffness characteristics depending on the walking phase. Therefore, we applied the proposed dynamic model based on the walking phase (or rotation direction). An inverted pendulum model was used during the stance phase, whereas a spring-loaded pendulum (SLP) model was utilized in the swing phase to simplify the real-time calculation of the multiple joint model. The SLP model was equipped with two virtual variables: virtual leg spring coefficient k_v and displacement d_v. In the swing model, we set k_v to 0.001, and d_v was calculated as; $d_v = D - \gamma_z$, where D is actual leg length, and γ_z is the distance between the hip joint and substrate. For the pectoral fins in the stance phase, the nonslip condition that assumes an ideal walking situation can be expressed as a kinematic constraint of contact position vector ($\mathbf{p}$) with respect to the earth-fixed frame $\{I\}$ as follows:

$$\mathbf{p}_{I\rm cp_i} = \text{const},\ \dot{\mathbf{p}}_{I\rm cp_i} = 0,\ \ddot{\mathbf{p}}_{I\rm cp_i} = 0. \tag{32}$$

To predict the traction force ($\mathbf{F}_{\rm gr}^{\rm st}$) in a stride following the given leg CPG trajectory, we calculated the inverse dynamics of the proposed equation of motion following the predicted inverted pendulum trajectory ($\boldsymbol{\gamma}(\rm t)$) under the nonslip condition

$$\begin{aligned} {}^B\mathbf{F}_{\rm gr}^{\rm st} = {} & [\mathbf{M}(\mathbf{q})\dot{\mathbf{u}}_\gamma]_B + [\mathbf{C}(\mathbf{u}_\gamma)\mathbf{u}_\gamma]_B + [\mathbf{D}(\mathbf{u}_\gamma)\mathbf{u}]_B \\ & + [g(\mathbf{q})]_B - {}^B\mathbf{F}_{\rm gr}^{\rm sw} \end{aligned} \tag{33}$$

where

$$\mathbf{u}_\gamma(t) = \mathbf{J}_B^{-1}\dot{\boldsymbol{\gamma}}(t) \tag{34}$$

$${}^B\mathbf{F}_{\rm gr}^{\rm sw} \approx \begin{bmatrix} k_v d_v \sin(q_i) - \mu k_v d_v \cos(q_i) \\ 0 \\ k_v d_v \cos(q_i) \end{bmatrix}. \tag{35}$$

To ensure a nonslip condition on the target substrate with a constant friction coefficient (μ), the $\mathbf{F}_{\rm gr}$ component in the normal direction of the substrate can be increased by the vertical component induced by the lateral fins, denoted as $(f_j^L)_z$. The downforce required by the lateral fins under a given slope can be calculated as follows:

$$\begin{aligned} & \max\left(\frac{1}{\mu}\sqrt{({}^B\mathbf{F}_{\rm gr}^{\rm st})_x^2 + ({}^B\mathbf{F}_{\rm gr}^{\rm st})_y^2} - ({}^B\mathbf{F}_{\rm gr}^{\rm st})_z\right) \\ & < \sum_{j=1}^{2} ({}^B f_{\rm j}^L)_z. \end{aligned} \tag{36}$$

D. Swimming Controller

The desired thrust ($\mathbf{F}_d$), which is manually set in the swimming mode, includes the desired forces (F_{xd}, F_{yd}, F_{zd}) and desired moments (M_{xd}, M_{yd}, M_{zd}) with respect to the surge, sway, and heave directions, respectively, given as follows:

$$\mathbf{F}_{\rm d} = \begin{bmatrix} F_{xd} & F_{yd} & F_{zd} & M_{xd} & M_{yd} & M_{zd} \end{bmatrix}^{\rm T}. \tag{37}$$

Based on the robot kinematics in Section III, the vector combinations of the four pectoral fins and two lateral fins can be formulated in a generalized form with the mapping matrix

Authorized licensed use limited to: POSTECH Library. Downloaded on August 30,2024 at 11:15:24 UTC from IEEE Xplore. Restrictions apply.

$\mathbf{A} \in \mathbb{R}^{6\times 14}$ and thrust vector $\mathbf{f}_{\mathrm{p}} \in \mathbb{R}^{1\times 14}$

$$\mathbf{A}\mathbf{f}_{\mathrm{p}} = \mathbf{F}_{\mathrm{d}} \tag{38}$$

where

$$\mathbf{f}_{\mathrm{p}} = \begin{bmatrix} f_{\mathrm{x}i} & f_{\mathrm{y}j} & f_{\mathrm{z}k} \end{bmatrix}^{\mathrm{T}} \tag{39}$$

$$\mathbf{A} = \begin{bmatrix} {}^{B}\hat{\mathbf{x}}_i & {}^{B}\hat{\mathbf{y}}_j & {}^{B}\hat{\mathbf{z}}_k \\ {}^{B}\mathbf{r}_{bi} \times {}^{B}\hat{\mathbf{x}}_i & {}^{B}\mathbf{r}_{bj} \times {}^{B}\hat{\mathbf{y}}_j & {}^{B}\mathbf{r}_{bk} \times {}^{B}\hat{\mathbf{z}}_k \end{bmatrix}. \tag{40}$$

For $\mathbf{A}$, the pectoral fins produce thrusts in the surge (f_x) and heave (f_z) directions ($i, k \in \{p_1 \dots p_4\}$), and the lateral fins produce thrusts in the surge, heave, and sway (f_y) directions ($i, j, k \in \{l_1, l_2\}$), and ${}^{B}\mathbf{r}$ is the position vector with respect to $\{B\}$. This underdetermined (or redundant) system formulated with $\mathbf{A}$ has infinite element combinations of $\mathbf{f}_{\mathrm{p}}$ and does not have a unique inverse matrix to satisfy the desired output $\mathbf{F}_{\mathrm{d}}$. We used the null-space projection method [60], [61] to determine $\mathbf{f}_{\mathrm{p}}$ by calculating the pseudoinverse matrix $\mathbf{A}^{+}$ to yield a solution that minimizes the cost function $\mathbf{H}_{\mathrm{cost}}$ with weight variables in surge (c_x) and heave (c_z) directions

$$\mathbf{f}_{\mathrm{p}} = \mathbf{A}^{+}\mathbf{F}_{\mathrm{d}} - (\mathbf{I} - \mathbf{A}^{+}\mathbf{A})\nabla\mathbf{H}_{\mathrm{cost}} \tag{41}$$

where

$$\mathbf{A}^{+} = \mathbf{A}^{\mathrm{T}}(\mathbf{A}\mathbf{A}^{\mathrm{T}})^{-1}\mathbf{F}_{\mathrm{d}} \tag{42}$$

$$\mathbf{H}_{\mathrm{cost}} = \sum_i (f_{\mathrm{x}i}^{P} + f_{\mathrm{z}i}^{P}) + \sum_j c_x(f_{\mathrm{x}j}^{L}) + c_z(f_{\mathrm{z}j}^{L}). \tag{43}$$

E. Buoyancy Control

The dynamic relationship between the control input of the ABCs and robot pose can be calculated by the momentum equation of the robot (19). In steady state, the robot pose satisfies the following moment balance equation:

$$\mathbf{r}_{bc} \times {}^{B}\mathbf{F}_{G} + \sum_{i=1}^{3} \mathbf{r}_{bb_i} \times {}^{B}\mathbf{F}_{a_i} = \mathbf{0}. \tag{44}$$

Assuming $\mathbf{r}_{\mathrm{bc}} = 0$, and the waist joint maintains its neutral position ($q_9 = \dot{q}_9 = 0$), the momentum equation can be simplified into a summarized form as follows:

$$\theta_{\mathrm{B}} = \arctan\left(\frac{\rho A g(l_{\mathrm{a2}} - l_{\mathrm{a1}})(d_{px} + k(l_{\mathrm{a2}} + l_{\mathrm{a1}})}{d_0 F_3}\right) \tag{45}$$

where the proportional constant k is 0.5. Then, the gravitational force applied to the body is expressed as follows:

$$[g(\mathbf{q})]_{\mathrm{B}}|_{x,y,z} = \begin{bmatrix} -(F_G - \sum_{i=0}^{2} F_{ai})\sin(\theta_B) \\ -(F_G - \sum_{i=0}^{2} F_{ai})\cos(\theta_B) \\ 0 \end{bmatrix}. \tag{46}$$

When the total buoyancy is kept constant ($l_{a1} + l_{a2}$), the robot can control the pitch angle to the target pitch angle (θ_{target}) through inverse dynamic calculation by determining the difference between the linear displacement of the front and rear ABCs ($\alpha = l_{a1} - l_{a2}$). The inverse dynamic operation is modified as follows:

$$a = -\frac{d_3 F_3 \tan(\theta_{\mathrm{target}})}{\rho A g(\mathrm{L} + k(l_{\mathrm{a1}} + l_{\mathrm{a2}}))} = K\tan(\theta_{\mathrm{target}}). \tag{47}$$

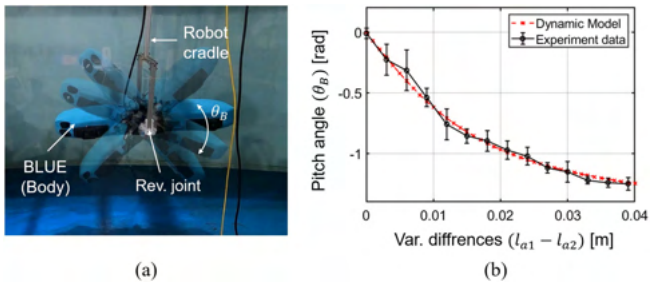

Fig. 9. Dynamic simulation and model validation of ABC. (a) Experimental setting for pitch angle control. (b) Simulation versus experimental data. The experimental data points and error bars represent the averages and standard deviations from three experiments.

Fig. 9(a) and (b) shows the experimental setting for pitch angle data measurement and a graph comparing the experimental pitch data with the proposed dynamic model results of the ABC, respectively. For the proposed dynamic model validation, we measured the robot pitch angle three times each for 14 buoyancy conditions, setting $l_{a2} = 0$, and increasing $l_{a1} = 0$ to 39 mm in 3-mm-intervals. We confirmed that the dynamic model of the proposed ABC exhibited a similar tendency to the actual experimental value.

V. Simulation Analysis

This section presents a multibody dynamic simulation that evaluates the passive mechanism of the pectoral fin during underwater legged locomotion. To determine the effectiveness of the pectoral fin during both walking and crawling, it is crucial to analyze GRF during both stance and swing phases. However, accurately measuring the GRF acting on the contact point of the pectoral fin can be challenging because it is difficult to install force sensors and angle encoders on the small-sized pectoral fin and passive joints. Moreover, BLUE has different positions and numbers of contact points with the substrate depending on its gait. To overcome this issue, we performed multibody rigid dynamic simulations for each legged gait and predicted the GRFs based on the proposed kinematic and dynamics models in Section III. The simulations were conducted in MATLAB Simulink environment with Simscape module. Table III summarizes the detailed simulation parameters and their values for the dynamic simulations. To account for the different number of contact points depending on the gait, we simulated walking by setting the contact point at the end of the pectoral fin to imitate contact with the substrate at the end of the leg. By contrast, during crawling motion, we simulated the potential contact points on each panel of the pectoral fin to imitate the occurrence of multiple contact points. The simulations and experiments were performed on a flat substrate with identical control inputs, and the experimental setup for acquiring the trajectory and hip torque data is described in Section VI. Fig. 10(a) and (b) compares a synchronized scene between the actual experiment and simulation, whereas Fig. 10(c) and (d) demonstrates the simulation and experimental results for walking and crawling gaits, respectively. Both the simulation and experiment results demonstrated consistent trends in trajectory and hip torque

Authorized licensed use limited to: POSTECH Library. Downloaded on August 30,2024 at 11:15:24 UTC from IEEE Xplore. Restrictions apply.

TABLE III
SIMULATION PARAMETERS USED FOR MULTIBODY DYNAMIC SIMULATIONS OF LEGGED LOCOMOTION

Parameter	Value	Unit	Parameter	Value	Unit
Total body mass	11.32	[kg]	Min. angle of ε_i ($\varepsilon_{\text{mini}}$)	$[0, 0, 0, 0, 0]$	[Deg]
Total buoyancy	100.23	[N]	Eq. angle of ε_i (ε_{eqi})	$[-10, -10, -10, 0, 0]$	[Deg]
Linear drag matrix ($\mathbf{K}_1^{\text{I}}$)	$\text{diag}({}^a\chi^{\text{I}}, 0, 9.34, 0.1, 0.1, 0.1)$	[N/m/s]	Spring coefficient (k_i)	$[0.08, 0.03, 0.01, 0.0035, 0.0015]$	[N·m]
Linear drag matrix ($\mathbf{K}_2^{\text{I}}$)	$\text{diag}(0, 0, 9.34, 0.1, 0.1, 0.1)$	[N/m/s]	Damping coefficient (c_i)	$[0.01, 0.01, 0.01, 0.01, 0.01]$	[N·cm/Deg/s]
Quadratic drag matrix ($\mathbf{K}_1^{\text{II}}$)	$\text{diag}({}^a\chi^{\text{II}}, 33.4, 93.43, 0.13, 0.13, 0.13)$	[N/m^2/s^2]	Friction coefficient (μ)	0.28	-
Quadratic drag matrix ($\mathbf{K}_2^{\text{II}}$)	$\text{diag}(0, 33.4, 93.43, 0.13, 0.13, 0.13)$	[N/m^2/s^2]	Position vector $\mathbf{r}_{bc}$	$[0, 0, 0.005]$	[m]

[a] For surge motions, the linear and quadratic drag coefficients ($\chi^{\text{I}}, \chi^{\text{II}}$) have distinct values depend on legged gait. For walking gait, the values of χ^{I} and χ^{II} are set to 1.38 and 20.73, respectively. For crawling gait, the values of χ^{I} and χ^{II} are set to 0.88 and 13.19, respectively.

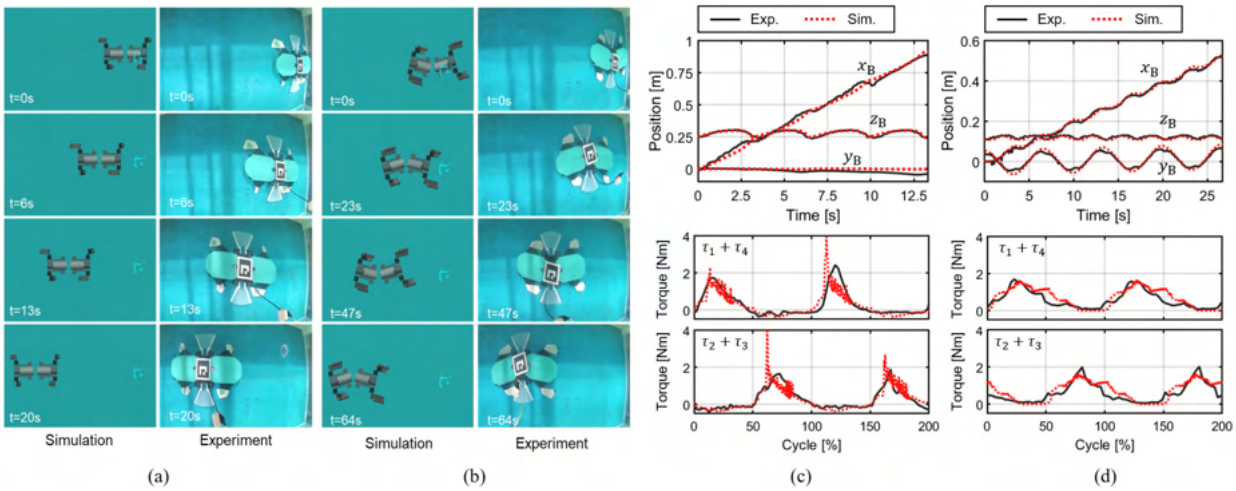

Fig. 10. Comparison of experimental and simulated motions in legged locomotion. (a) Walking gait. (b) Crawling gait. The simulation results (red dotted line) of (c) walking gait and (d) crawling gait show similar values compared with experiment data (black line) of robot trajectories in surge, sway, and heave directions and hip joint torque.

values for both walking and crawling gaits, indicating good coherence of the proposed dynamic model. Fig. 11 shows the active and passive joint trajectories and the simulated GRFs in the normal and tangential directions for walking and crawling gaits, respectively, over a gait cycle. During the walking/crawling gait, pectoral fins interact with the substrate and change the stance and swing phases by passively inducing different GRFs depending on the rotation direction of the hip joint. In the stance and swing phases, the hip joints require relatively high and low torques to induce enough GRFs to lift the robot and move the pectoral fin for the next stride, respectively. The simulation results show that the anisotropic mechanical feature contributed to the creation of repetitive and stable stance/swing phase transition in both walking and crawling gaits. During both gaits, the hip joint torque can be clearly distinguished between the stance and swing phases, thereby indicating the changes in GRF over each stride in the simulation results.

VI. EXPERIMENT AND RESULT

The hybrid mobility and robustness of BLUE were investigated by conducting the following experiments in a water tank environment:

1) thrust experiment of proposed bioinspired fins;
2) underwater legged locomotion test on gravel substrate in the water;
3) underwater legged locomotion test in an environment with currents;
4) robustness test of walking gait on slope in the water.

The indoor experiments were implemented in a 1.5 × 3 × 1.7 m (width × length × height) water tank. For the thrust experiments, force data were acquired at 125 Hz sampling rates by fixing a multiaxis torque sensor to the water tank frame. In the legged locomotion experiments, the robot's 3-D position trajectory was measured using a vision-based marker detection method [62] with on-site calibration via a fish-eye monitoring camera installed in the upper part of the water tank frame. Table IV shows the CPG control inputs for generating legged motions in each experiment.

A. Thrust Test of Bioinspired Fins and Swimming Trial

Detailed swimming capability verification was conducted in two ways. Quantitative thrust experiments and analysis were performed at the bioinspired fin level, followed by a feasibility

Authorized licensed use limited to: POSTECH Library. Downloaded on August 30,2024 at 11:15:24 UTC from IEEE Xplore. Restrictions apply.

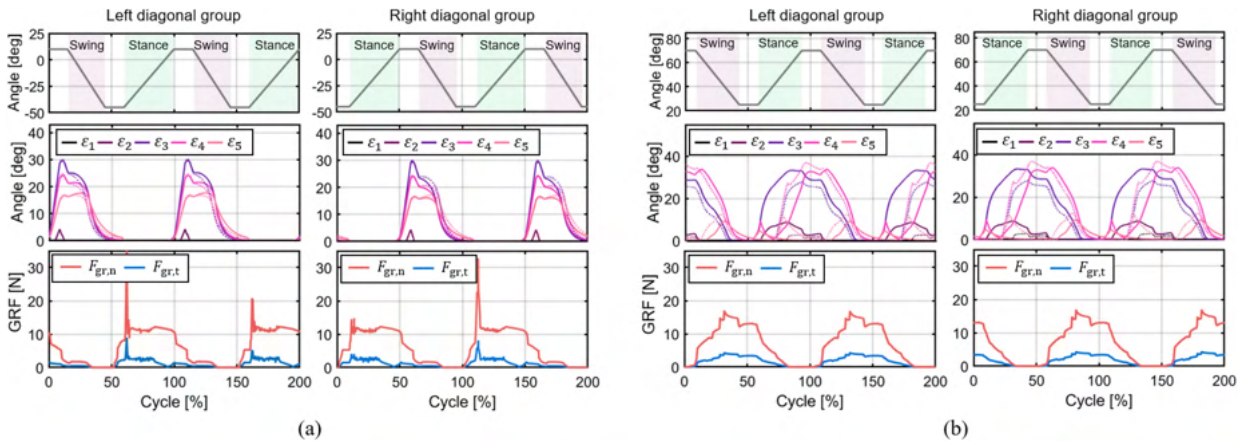

Fig. 11. Multibody dynamics simulation results of the proposed legged locomotion. (a) Walking gait. (b) Crawling gait. These figures highlight the trajectory inputs of the hip joint, the passive joint trajectories, and the GRF induced at the contact point of the pectoral fin, depending on the gait cycle. The values $F_{gr,n}$ and $F_{gr,t}$ denote the GRF element in the normal and tangential direction, respectively. In crawling gait, the total GRF generated by various contact points is calculated. The induced GRF exhibits a regular and repetitive pattern with respect to the gait phase, significantly correlating with the input torque illustrated in Fig. 10(a) and (b).

TABLE IV
CONTROL PARAMETERS FOR LEGGED LOCOMOTION EXPERIMENTS

Gait	f [Hz]	$q_{\min}$ [deg]	$q_{\max}$ [deg]	γ_{st} [-]	γ_{sw} [-]
Walking (F, C)	0.15	−45	10	0.4	0.3
Crawling (F, C)	0.15	25	70	0.35	0.35
Walking (G)	0.18	−45	10	0.4	0.3
Crawling (G)	0.18	25	70	0.35	0.35
Walking (S)	0.12	−45	24	0.35	0.35

F, G, C, and S denote flat, gravel, current, and slope, respectively.

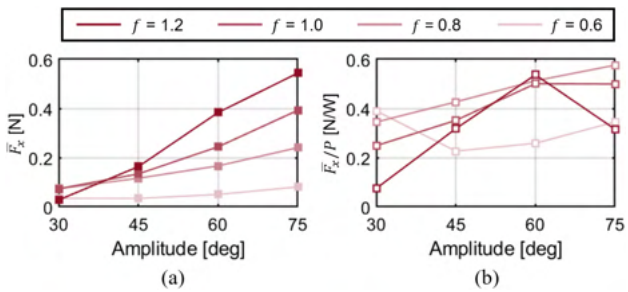

Fig. 12. Thrust experiments of pectoral fin. (a) Average thrust. (b) Electrical efficiency in oscillating motion.

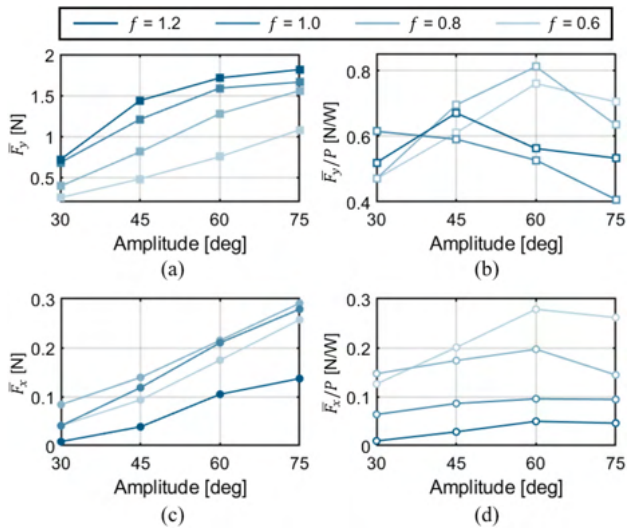

Fig. 13. Thrust experiments of lateral fin. (a) Average thrust. (b) Electrical efficiency in oscillating motion. (c) Average thrust. (d) Electrical efficiency in undulating motion with 0.5π phase shift.

test of swimming at the robot level.[1] Figs. 12 and 13 show the average thrust and electrical efficiency according to the motion of the pectoral and lateral fins, respectively. The generated thrust results of the pectoral and lateral fins demonstrated different characteristics depending on the swimming motions. Unlike the oscillating motion, which has a proportional relationship with the oscillating frequency and thrust, the undulating motion achieved poor thrust when controlled over 1 Hz. The oscillation of the pectoral fin had a relatively high thrust compared to that of the undulating lateral fin. Based on the distinctive thrust results, BLUE used the following strategies to swim: Because the pectoral fin is suitable for moving the body at high speed by exerting strong thrust in the surge, it is the main thrust module for fast movement with relatively low accuracy [see Fig. 14(a)]. Conversely, the lateral fin can move the body at low acceleration and high accuracy [see Fig. 14(b)], and can easily change the thrust direction in the surge by changing the phase offset. In addition, the lateral fin can generate thrust in the sway direction by oscillating motion [see Fig. 14(c)] and is suitable for precise movements, such as positioning in the surge and sway directions.

[1][Online]. Available: https://ieeexplore.ieee.org. This shows the swimming trials of BLUE in a water tank.

Authorized licensed use limited to: POSTECH Library. Downloaded on August 30,2024 at 11:15:24 UTC from IEEE Xplore. Restrictions apply.

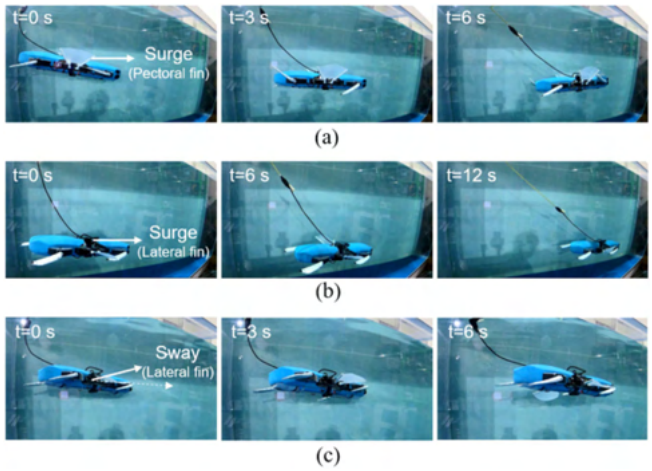

Fig. 14. Swimming trials in water tank: forward (surge) movement using (a) only the pectoral fin group and (b) lateral fin group. (c) Side (sway) movement using only the lateral fin group.

B. Underwater Locomotion on Gravel Terrain

In this experiment, we demonstrated that pectoral fins are sufficient as limbs for underwater-legged locomotion (walking and crawling) and confirmed the robustness of both gaits on atypical substrates. In the locomotion test on the gravel terrain, the testbed was 3 m long, and a flat terrain was maintained approximately 1.3 m in front of the testbed. The gravel was installed in the remaining rear part. The gravel terrain comprised gravel ranging from 3 to 5.5 cm in diameter, forming an obstacle with a maximum height of 30% of the total length of the limb (pectoral fin). Fig. 15 shows the walking and crawling results on the gravel terrain comprehensively. The 3-D visualized path and time trajectories [see Fig. 15(a)] show the robustness of BLUE on the atypical substrate represented by gravel depending on the walking and crawling gaits. In the flat zone, the robot moved forward with repeated actions and directions in both gaits. However, in the gravel zone, the robot overcame the gravel obstacles and reached the end line only through the walking gait. The crawling gait exhibited decreased speed and was unstable in the crawling direction when traversing the gravel terrain, whereas the walking gait maintained the walking speed and direction. This result is also reflected in the regularity of hip torque over the strides [see Fig. 15(b) and (c)]. In the walking gait, the stance/swing phases were easily distinguishable in both flat and gravel areas, and the regularity of torque was maintained even in the gravel area. However, the crawling gait showed instability in its gait pattern and disrupted regularity in phase, specifically in the gravel terrain. The results indicate that the walking gait, characterized by a high robot height and large stride, is more robust in gravel terrain than the crawling gait. Note that without prior information on the terrain, BLUE fully negotiated the gravel substrate without a noticeable delay in walking speed using the walking gait owing to the passive bending mechanism of the pectoral fin (see Fig. 16).[2]

C. Underwater Locomotion in Current

Locomotion in water currents remains an open challenge in underwater robotics. Previous studies have presented legged robot platforms as a feasible solution to achieve station keeping or locomotion underwater flow disturbances through interaction between the limbs and seabed. However, few legged robot platforms have shown seabed locomotion with underwater flow disturbances by quantitative experiments. In this experiment, to quantitatively confirm the feasibility of seabed locomotion against water flow, BLUE performed walking and crawling in an indoor environment where three levels of flows (high, mid, and low) existed (see Figs. 17–19).[3] The surface of the testbed was flat and slippery, and the friction coefficient between the surface and BLUE was less than 0.3. For the locomotion test in various environments with currents, a custom-developed water current generator with three levels of artificial water flows was applied to the bottom of the water tank according to the flow intensity. Figs. 17 and 18(a) and (b) show the 2-D paths (top-view) and time trajectories of the walking and crawling gaits under various currents, respectively. The 2-D path results indicated that the crawling motion overcame the water current better than the walking motion. The lagging phenomena during each gait clearly indicated that the robot moved more robustly amidst the current via the crawling gait. In low flow, both gaits overcame the water current and reached the end line (1.7 m from the start line). However, the walking gait exhibited a time lag of 10.7%, whereas the crawling gait did not cause a significant time lag compared with the locomotion trajectories without water flow. In mid-flow, the walking gait failed to reach the end line (approximately 1.4 m from the start line), whereas the crawling gait reached the end line. In addition, the lagging value calculated based on a distance of 1.2 m from the start line showed a lower value in crawling (10.5%) than in walking (44.6%). Finally, in high flow, neither of the gaits reached the end line; however, the robot with the walking gait was swept away and failed around 0.5 m, whereas the crawling robot continuously crawled in place while maintaining a heading around 1.2 m. These experiments confirmed that the crawling gait exhibited a higher ability to overcome water flow than the walking gait. We suggest two possible reasons for the high robustness of the crawling gait in water flow. First, the average height and cross-sectional area in the surge direction were 26% lower in the crawling gait than in the walking gait, which decreased the water flow resistance. This is in line with the behavior of rock-climbing fish [49] or benthic animals, such as crabs, lobsters, or crayfishes, which lower and lean their bodies in torrential flow [63], [64]. Second, the contact points or areas changed according to the locomotion posture. During crawling gait, the bent pectoral fin interacts with the substrate with the paddle surface. The numerous contact points and extensive contact area with the substrate can effectively mitigate momentary slippage phenomena, ultimately aiding in maintaining posture.

[2][Online]. Available: https://ieeexplore.ieee.org. This shows the side view of BLUE during underwater walking on gravel substrate.

[3][Online]. Available: https://ieeexplore.ieee.org. This shows the top view of BLUE during underwater legged locomotion under various water flows.

Authorized licensed use limited to: POSTECH Library. Downloaded on August 30,2024 at 11:15:24 UTC from IEEE Xplore. Restrictions apply.

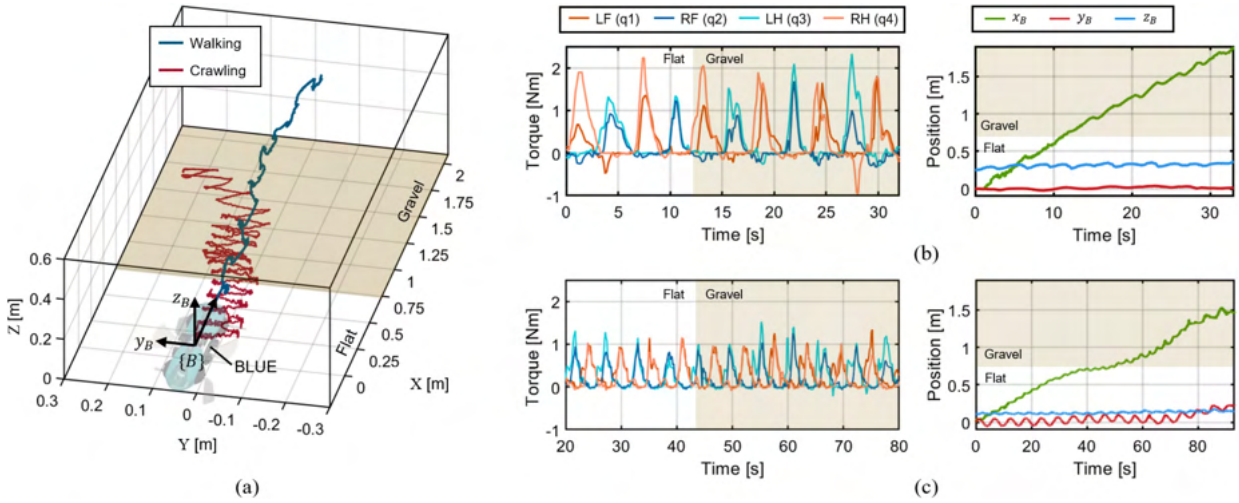

Fig. 15. Underwater legged locomotion test on flat and gravel substrate. (a) 3-D path of BLUE in walking and crawling gaits. (b) Hip joint torque and time trajectory of BLUE in (b) walking gait and (c) crawling gait. 3-D position data in surge, sway, and heave directions are recorded by the monitoring camera with calibration, and hip torques are calculated using current data recorded by on-board sensors of servos.

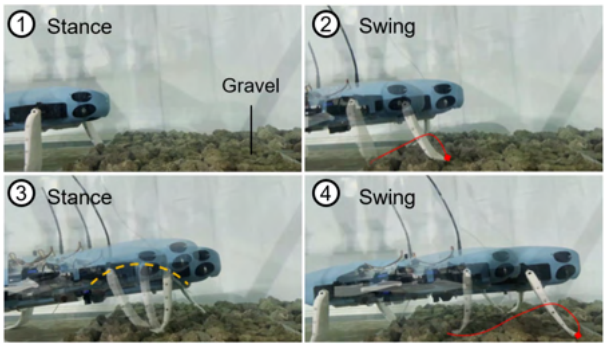

Fig. 16. Snapshots of BLUE while underwater walking on gravel substrate.

D. Underwater Locomotion in Slope Terrain

Walking on a slope is not commonly attempted in aquatic environments, considering most aquatic animals can swim. However, within the domain of robotics applications, the attributes inherent to legged motion, such as consistent movement and station-keeping, can be used importantly in underwater sensing missions that require precise substrate observation or maneuvering across various terrains, including slopes. For example, during underwater inspections in rocky or hilly environments, which are commonly encountered underwater, or 3-D reconstruction missions of underwater structures or shipwrecks, slope walking enhances the robustness and versatility of walking gait. This capability allows BLUE to overcome large obstacles over step size or stably move over steep terrain. Nonetheless, to achieve slope walking, the robot requires sufficient attachment force at the contact point with the substrate to ensure a stable gait and posture. On flat or low slopes, the primary attachment force acting in the normal direction (downforce) is provided by the gravitational force. However, as the slope of the terrain increases, this force converts to a shear direction force, resulting in a slip at the contact point or even causing the robot to roll over. To counteract this, an additional downforce is required on a steep slope by offsetting the gravitational force with buoyancy to reduce the robot's slip and increase posture stability. The slope walking motion of BLUE is based on the walking gait and utilizes the two lateral fins and ABCs with the slope feedback subcontroller. In the climbing test, we created a 30° slope using an aluminum frame and PVC plank at the bottom of the tank. We conducted a comparative experiment by categorizing the cases based on the robot's lateral paddling and buoyancy control operation.[4] Figs. 20 and 21 show the experimental results according to each case. When using pectoral fins (Case A), BLUE was unable to climb the slope owing to the slip and postural instability caused by the high gravitational force [see Fig. 21(a)]. By incorporating lateral fin paddling into the walking gait (Case B), the maximum body rotation amplitude in the roll and pitch directions decreased by 38.0% and 24.9%, respectively. Nevertheless, the slip was not eliminated because the downforce was insufficient to satisfy the nonslip conditions required for the gait in water [see Figs. 21(b) and 22(a)]. The slip condition can be mitigated by offsetting the gravitational element in the shear direction through buoyancy control (Case C). Consequently, BLUE successfully overcame the slip problem and negotiated the steep slope [see Figs. 21(c) and 22(b)].

VII. Field Trials

For quantitative evaluation, BLUE was tested in a water tank with various measurement sensors and artificial obstacles. However, to verify whether BLUE is capable of performing the proposed hybrid motion in real-life environments, we conducted field trials for each locomotion mode.[5] The swimming capability

[4][Online]. Available: https://ieeexplore.ieee.org. This shows the side view of BLUE during the climbing comparison test.

[5][Online]. Available: https://ieeexplore.ieee.org. This shows field validations of BLUE's multimodal capability.

Authorized licensed use limited to: POSTECH Library. Downloaded on August 30,2024 at 11:15:24 UTC from IEEE Xplore. Restrictions apply.

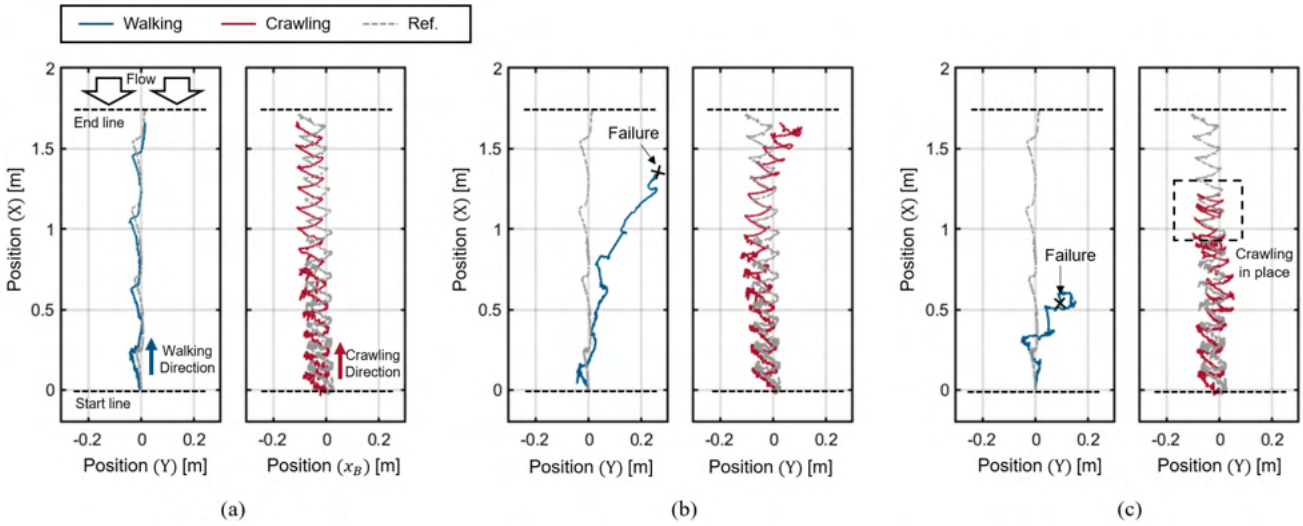

Fig. 17. 2-D Path of BLUE utilizing walking and crawling gait according to the water flow intensity. (a) Low flow. (b) Middle flow. (c) High flow. Ref. means the reference path of walking and crawling gait in none-flow environment.

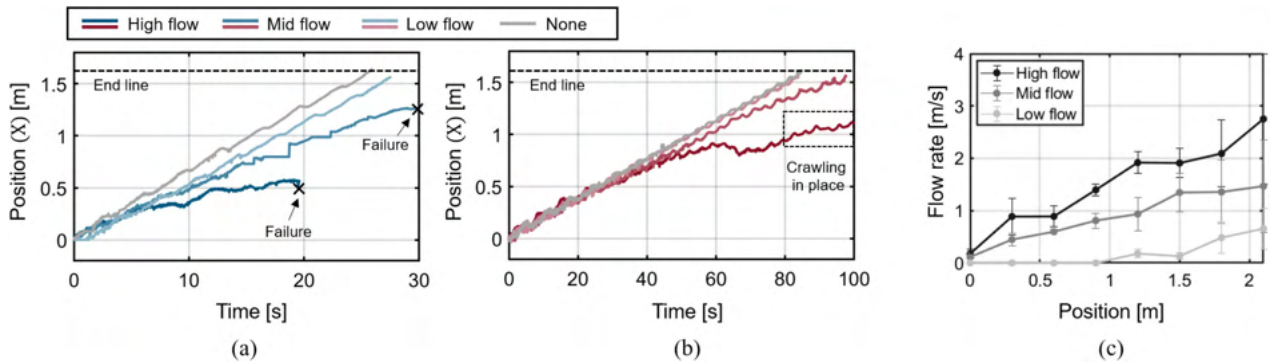

Fig. 18. Time trajectories visualized in surge of (a) walking gait and (b) crawling gait according to the water flow intensity. (c) Average flow rates at the bottom side depend on the distance from the start line. The flow rates were measured by flow meter at 24 points in eight rows and three columns.

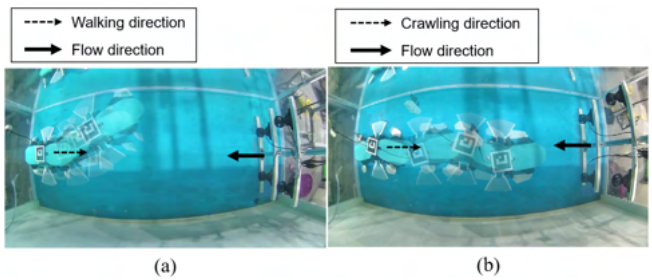

Fig. 19. Overlapped sequential photos of BLUE with (a) walking and (b) crawling gaits in high water flow on slippery surface.

of BLUE was tested in an open sea environment, whereas its walking, crawling, and climbing capabilities were tested in a lake or stream bed. As shown in Fig. 23(a), in the swimming trials, BLUE exhibited a natural and smooth movement, utilizing both undulating and oscillating motion of the bioinspired fins to move through a 3-D space, resembling an aquatic creature. In the legged locomotion experiments, BLUE could withstand water currents under 0.2 m/s, traverse a rough substrate of gravel [see Fig. 23(b)], and negotiate a slippery rock slope with a gradient exceeding 20° [see Fig. 23(c)]. Moreover, BLUE successfully crawled on a seaweed-covered slippery floor with water flow disturbances exceeding 0.4 m/s [see Fig. 23(d)]. These results demonstrate the adaptability of BLUE to diverse underwater environments and overcome challenges through its hybrid locomotion capabilities.

VIII. Discussion

A. CoT Calculation

The electrical or metabolic CoT for both walking and crawling gaits was calculated according to [30]: $\mathrm{CoT} = \bar{P}_{\mathrm{in}}/mg\bar{v}$. The mass of our robot (m) was 11.32 kg, and the gravity acceleration g was 9.81 m/s. The electrical power input ($\bar{P}_{\mathrm{in}}$) was obtained by summing the power (in watts) of each actuator used for robot operation. To calculate the individual motor power, the individual input voltage (V) and instantaneous current (I)

Authorized licensed use limited to: POSTECH Library. Downloaded on August 30,2024 at 11:15:24 UTC from IEEE Xplore. Restrictions apply.

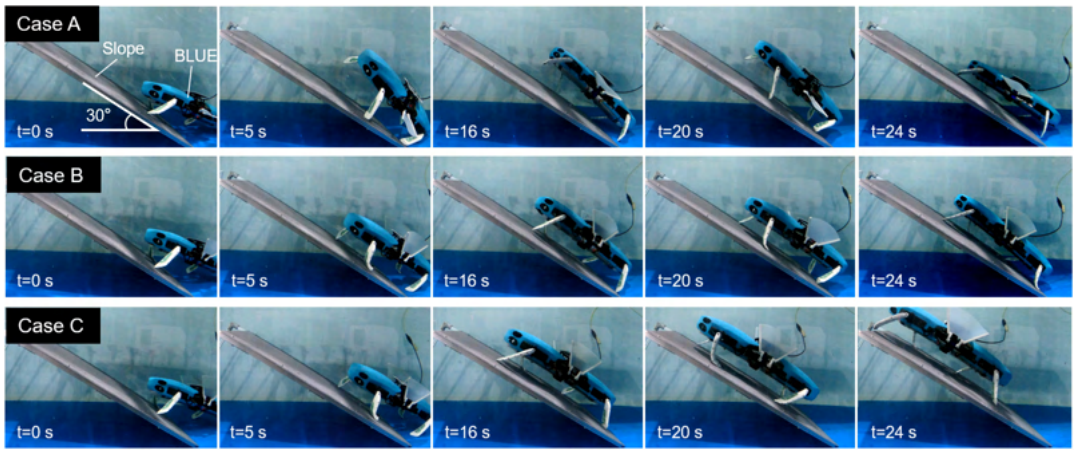

Fig. 20. Climbing comparison test on 30° slope. Climbing using normal walking gait (Case A), climbing using a walking gait with lateral fin oscillation (Case B), and climbing using a walking gait with lateral fin oscillation and buoyancy optimizing from −1.1 to −0.2 kg in underwater weight (Case C).

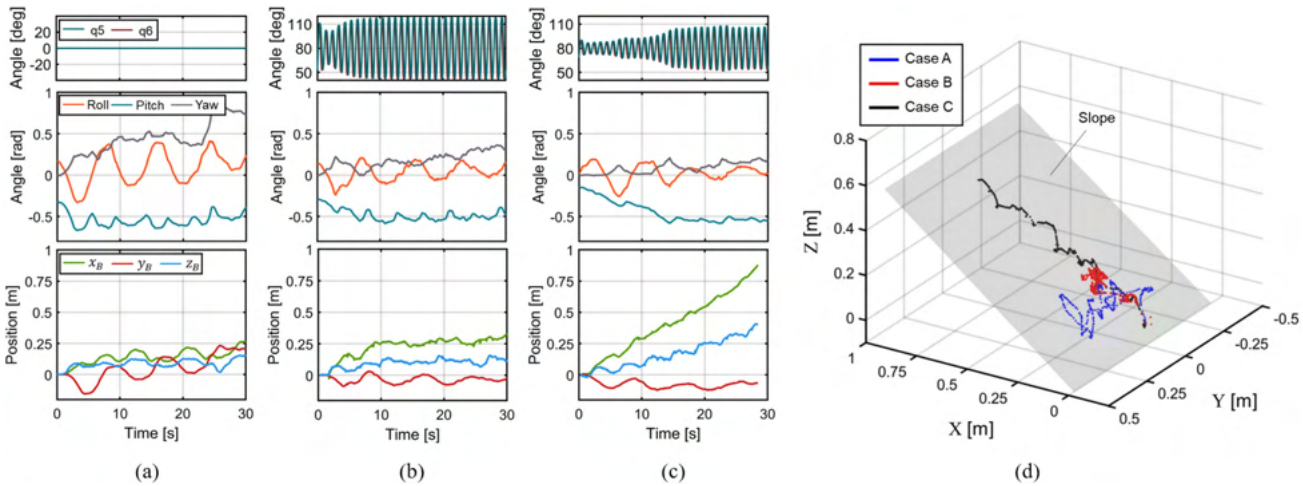

Fig. 21. Control inputs of lateral fins and slope walking experiment results according to case. (a) Case A. (b) Case B. (c) Case C. The experiment results contain time trajectories of BLUE in inertial coordinates and pose data in roll, pitch, and yaw directions. (d) 3-D path of BLUE according to case.

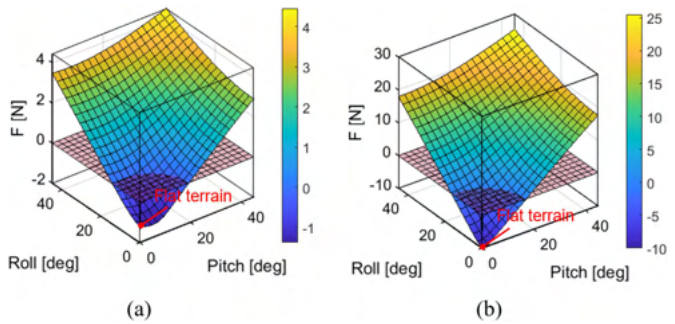

Fig. 22. Required downforce according to the robot's roll and pitch posture to meet nonslip conditions of −1.1 kgf (a) and −0.2 kgf (b) underwater weight.

were measured by an electric gauge that was built into each actuator and calibrated to fit the unit. In the electric power calculation, we disregarded the standby power (0.48 W for each actuator). The average velocity $\bar{v}$ of the robot was obtained through locomotion experiments for walking and crawling gaits in flat terrain without water flow. The CoT values for both walking (0.18 Hz) and crawling (0.18 Hz) gait were calculated based on three identical-condition experiments. For walking gait, the average CoT was 0.827 (maximum: 0.852, minimum: 0.805), with a standard deviation of 0.024. In crawling gait, the average CoT was 3.813 (maximum: 3.894, minimum: 3.677), with a standard deviation of 0.119. In future works, optimizing the walking/crawling trajectory function may improve the CoT value.

B. Potential Applications

BLUE can be applied to a wide range of real-life underwater environments owing to its various locomotion functions and bioinspired design. In a harsh aquatic environment, where it is difficult to apply traditional thrust-driven ROVs or AUVs, legged motions can help effectively overcome environmental obstacles, such as shallow water with current and narrow spaces

Authorized licensed use limited to: POSTECH Library. Downloaded on August 30,2024 at 11:15:24 UTC from IEEE Xplore. Restrictions apply.

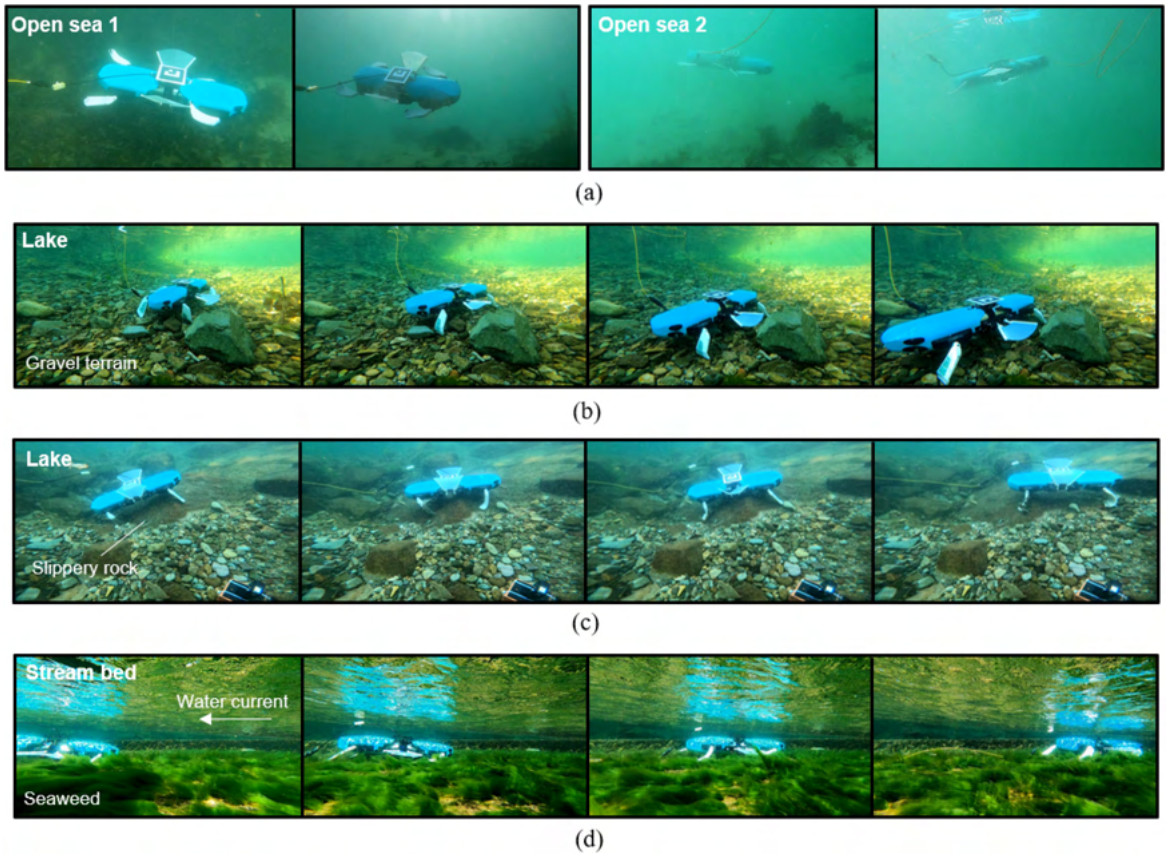

Fig. 23. Field validations of BLUE's multimodal capability. (a) Swimming using multiple fins in open sea. (b) Walking on gravel terrain. (c) Walking on slippery rock slope. (d) Crawling on seaweed amidst water flow.

TABLE V
COMPARISON WITH NONPROPELLER-DRIVEN UNDERWATER MULTIMODAL ROBOTS

Name	Mass	Buoy. control	Underwater gait			Land gait	Covering underwater substrate
			Walking	Swimming	Etc.		
HERO-BLUE	11.32 kg	✓ (1.2 kgf)	✓ (62.5 mm/s)	✓ (300 mm/s)	Crawling (21.2 mm/s)	-	F, G, S, M
ART [30]	9 kg	-	-	✓ (83.3 mm/s)	-	✓ (29.0 mm/s)	-
SILVER-II [18]	22 kg	-	✓ (54.5 mm/s)	-	Hopping (87.0 mm/s)	-	F, G, M
Salamandra robotica II [66]	2.5 kg	-	-	✓ (510 mm/s)	-	✓ (420 mm/s)	-
CR-200 [67]	600 kg	-	✓ (500 mm/s)	✓ (N/A)	-	-	F
PEAR [31]	7.15 kg	✓ (0.45 kgf)	✓ (32.5 mm/s)	✓ (N/A)	-	-	F, G, S, M
Glide Walker [68]	1.06 kg	-	✓ (60 mm/s)	✓ (470 mm/s)	-	-	F
AmphiHex-II [36]	14 kg	-	-	✓ (180 mm/s)	-	✓ (350 mm/s)	-

Substrate labeled as F corresponds to flat, G corresponds to gravel, S corresponds to slope , and M corresponds to seaweed and mud.

with complex structures, such as ropes or rock. Table V provides a clear depiction of BLUE's potential compared to similar nonpropeller-driven bioinspired robots. BLUE demonstrates superior underwater mobility and functionality, showcasing its capabilities for effectively covering various underwater terrains. Furthermore, BLUE's nonthreatening presence to aquatic organisms, owing to its bioinspired design and movements, can position it as an ideal tool for active exploration of marine ecosystems, which can provide crucial information about the Earth. In contrast, traditional thruster-propelled robots can damage underwater flora and fauna with blades, leave considerable biofootprints, and destroy the marine environment. In addition, conventional propeller-based underwater robots frequently endure the entanglement of marine debris and seaweed in their blades during nearshore missions. These propellers might pose a risk to divers in human-ROV collaborative missions. In terms

Authorized licensed use limited to: POSTECH Library. Downloaded on August 30,2024 at 11:15:24 UTC from IEEE Xplore. Restrictions apply.

of mobility, the proposed walking and swimming mechanism of BLUE offers a promising solution to these difficulties.

IX. Conclusion

This study proposed a novel bioinspired underwater robot platform, HERO-BLUE that demonstrated multimodal locomotion capabilities, including swimming, walking, and crawling. Our platform features multimodal fins with numerous passive joints, a salamander-like spine, and soft undulating fins that enable efficient and robust locomotion in diverse aquatic environments. We presented mathematical models, motion planning methodology, and control strategies for achieving hybrid motions. Our water tank experiments and field experiments in various scenarios showed that the proposed platform could successively combine swimming and legged motion capability and demonstrate versatility in various environments. The hybrid mobility of BLUE can potentially be applied in various real-life underwater applications that require flexible behaviors during missions. In future works, we intend to conduct a comprehensive analysis of the mechanisms underlying the coupled motion between fins, aiming to deepen our understanding and improve the overall effectiveness of our approach.

Acknowledgment

The authors would like to thank Dr. Minsung Sung, Seokyong Song, Young-Woon Song, Jason Kim, and Ingyu Lee for their valuable advice and support.

References

[1] M. D. Smith et al., "Sustainability and global seafood," *Science*, vol. 327, no. 5967, pp. 784–786, 2010.
[2] A. Couper, *The Geography of Sea Transport*. Evanston, IL, USA: Routledge, 2015.
[3] T. Wilberforce, Z. El Hassan, A. Durrant, J. Thompson, B. Soudan, and A. G. Olabi, "Overview of ocean power technology," *Energy*, vol. 175, pp. 165–181, 2019.
[4] F. Hu, Y. Huang, Z. Xie, J. Yu, Z. Wang, and J. Qiao, "Conceptual design of a long-range autonomous underwater vehicle based on multidisciplinary optimization framework," *Ocean Eng.*, vol. 248, 2022, Art. no. 110684.
[5] Z. Chu, F. Wang, T. Lei, and C. Luo, "Path planning based on deep reinforcement learning for autonomous underwater vehicles under ocean current disturbance," *IEEE Trans. Intell. Veh.*, vol. 8, no. 1, pp. 108–120, Jan. 2023.
[6] J. Pyo, H. Cho, H. Joe, T. Ura, and S.-C. Yu, "Development of hovering type AUV "cyclops" and its performance evaluation using image mosaicing," *Ocean Eng.*, vol. 109, pp. 517–530, 2015.
[7] L. Zacchini, M. Franchi, and A. Ridolfi, "Sensor-driven autonomous underwater inspections: A receding-horizon RRT-based view planning solution for AUVs," *J. Field Robot.*, vol. 39, no. 5, pp. 499–527, 2022.
[8] D. R. Yoerger et al., "A hybrid underwater robot for multidisciplinary investigation of the ocean twilight zone," *Sci. Robot.*, vol. 6, no. 55, 2021, Art. no. eabe1901.
[9] R. Duan, J. Du, C. Jiang, and Y. Ren, "Value-based hierarchical information collection for AUV-enabled Internet of Underwater Things," *IEEE Internet Things J.*, vol. 7, no. 10, pp. 9870–9883, Oct. 2020.
[10] J. Kim, T. Kim, S. Song, M. Sung, and S.-C. Yu, "Parent-child underwater robot-based manipulation system for underwater structure maintenance," *Control Eng. Pract.*, vol. 134, 2023, Art. no. 105459.
[11] E. Galceran, R. Campos, N. Palomeras, D. Ribas, M. Carreras, and P. Ridao, "Coverage path planning with real-time replanning and surface reconstruction for inspection of three-dimensional underwater structures using autonomous underwater vehicles," *J. Field Robot.*, vol. 32, no. 7, pp. 952–983, 2015.
[12] S. Okada, K. Hirano, P. Jp, R. Kobayashi, and Y. Kometani, "Development and application of robotics for decommissioning of Fukushima Daiichi nuclear power plant," *Hitachi Rev*, vol. 69, no. 4, pp. 556–557, 2020.
[13] M. Nancekievill et al., "Development of a radiological characterization submersible ROV for use at Fukushima Daiichi," *IEEE Trans. Nucl. Sci.*, vol. 65, no. 9, pp. 2565–2572, Sep. 2018.
[14] J. Wu et al., "Multi-AUV motion planning for archeological site mapping and photogrammetric reconstruction," *J. Field Robot.*, vol. 36, no. 7, pp. 1250–1269, 2019.
[15] R. Wang, S. Wang, Y. Wang, L. Cheng, and M. Tan, "Development and motion control of biomimetic underwater robots: A survey," *IEEE Trans. Syst., Man, Cybern. Syst.*, vol. 52, no. 2, pp. 833–844, Feb. 2022.
[16] O. Guetta, D. Shachaf, R. Katz, and D. Zarrouk, "A novel wave-like crawling robot has excellent swimming capabilities," *Bioinspiration Biomimetics*, vol. 18, 2023, Art. no. 026006.
[17] D. Romano and C. Stefanini, "Any colour you like: Fish interacting with bioinspired robots unravel mechanisms promoting mixed phenotype aggregations," *Bioinspiration Biomimetics*, vol. 17, no. 4, 2022, Art. no. 045004.
[18] G. Picardi, M. Chellapurath, S. Iacoponi, S. Stefanni, C. Laschi, and M. Calisti, "Bioinspired underwater legged robot for seabed exploration with low environmental disturbance," *Sci. Robot.*, vol. 5, no. 42, 2020, Art. no. eaaz1012.
[19] J. Liu, S. Iacoponi, C. Laschi, L. Wen, and M. Calisti, "Underwater mobile manipulation: A soft arm on a benthic legged robot," *IEEE Robot. Automat. Mag.*, vol. 27, no. 4, pp. 12–26, Dec. 2020.
[20] E. Kelasidi, P. Liljebäck, K. Y. Pettersen, and J. T. Gravdahl, "Integral line-of-sight guidance for path following control of underwater snake robots: Theory and experiments," *IEEE Trans. Robot.*, vol. 33, no. 3, pp. 610–628, Jun. 2017.
[21] E. Kelasidi, P. Liljeback, K. Y. Pettersen, and J. T. Gravdahl, "Innovation in underwater robots: Biologically inspired swimming snake robots," *IEEE Robot. Autom. Mag.*, vol. 23, no. 1, pp. 44–62, Mar. 2016.
[22] X. Jiang, F. Yang, and S. Shi, "Design and full-link trajectory tracking control of underwater snake robot with vector thrusters under strong time-varying disturbances," *Ocean Eng.*, vol. 266, 2022, Art. no. 113012.
[23] M. Wu et al., "Glowing sucker octopus (stauroteuthis syrtensis)-inspired soft robotic gripper for underwater self-adaptive grasping and sensing," *Adv. Sci.*, vol. 9, no. 17, 2022, Art. no. 2104382.
[24] Q. Wu et al., "A novel underwater bipedal walking soft robot bio-inspired by the coconut octopus," *Bioinspiration Biomimetics*, vol. 16, no. 4, 2021, Art. no. 046007.
[25] A. S. Lafmejani et al., "Kinematic modeling and trajectory tracking control of an octopus-inspired hyper-redundant robot," *IEEE Robot. Autom. Lett.*, vol. 5, no. 2, pp. 3460–3467, Apr. 2020.
[26] P. Duraisamy, R. Kumar Sidharthan, and M. Nagarajan Santhanakrishnan, "Design, modeling, and control of biomimetic fish robot: A review," *J. Bionic Eng.*, vol. 16, no. 6, pp. 967–993, 2019.
[27] R. K. Katzschmann, J. DelPreto, R. MacCurdy, and D. Rus, "Exploration of underwater life with an acoustically controlled soft robotic fish," *Sci. Robot.*, vol. 3, no. 16, 2018, Art. no. eaar3449.
[28] H. Shao et al., "Thrust improvement of a biomimetic robotic fish by using a deformable caudal fin," *Biomimetics*, vol. 7, no. 3, 2022, Art. no. 113.
[29] K. Kim, P. Spieler, E.-S. Lupu, A. Ramezani, and S.-J. Chung, "A bipedal walking robot that can fly, slackline, and skateboard," *Sci. Robot.*, vol. 6, no. 59, 2021, Art. no. eabf8136.
[30] R. Baines et al., "Multi-environment robotic transitions through adaptive morphogenesis," *Nature*, vol. 610, no. 7931, pp. 283–289, 2022.
[31] T. Kim, Y.-w. Song, S. Song, and S.-C. Yu, "Underwater walking mechanism of underwater amphibious robot using hinged multi-modal paddle," *Int. J. Control, Autom. Syst.*, vol. 19, no. 4, pp. 1691–1702, 2021.
[32] U. Saranli, M. Buehler, and D. E. Koditschek, "Rhex: A simple and highly mobile hexapod robot," *Int. J. Robot. Res.*, vol. 20, no. 7, pp. 616–631, 2001.
[33] G. Dudek et al., "Aqua: An amphibious autonomous robot," *Computer*, vol. 40, no. 1, pp. 46–53, 2007.
[34] B. B. Dey, S. Manjanna, and G. Dudek, "Ninja legs: Amphibious one degree of freedom robotic legs," in *Proc. IEEE/RSJ Int. Conf. Intell. Robots Syst.*, 2013, pp. 5622–5628.
[35] L. Bai, G. Dou, W. Duan, Y. Sun, J. Zheng, and X. Chen, "Amphibious robot with a novel composite propulsion mechanism," in *Proc. IEEE 6th Int. Conf. Adv. Robot. Mechatron.*, 2021, pp. 442–447.

Authorized licensed use limited to: POSTECH Library. Downloaded on August 30,2024 at 11:15:24 UTC from IEEE Xplore. Restrictions apply.

[36] B. Zhong, S. Zhang, M. Xu, Y. Zhou, T. Fang, and W. Li, "On a CPG-based hexapod robot: AmphiHex-II with variable stiffness legs," *IEEE/ASME Trans. Mechatron.*, vol. 23, no. 2, pp. 542–551, Apr. 2018.
[37] S. Zhang, Y. Zhou, M. Xu, X. Liang, J. Liu, and J. Yang, "AmphiHex-I: Locomotory performance in amphibious environments with specially designed transformable flipper legs," *IEEE/ASME Trans. On Mechatron.*, vol. 21, no. 3, pp. 1720–1731, Jun. 2016.
[38] X. Ma, G. Wang, and K. Liu, "Design and optimization of a multimode amphibious robot with propeller-leg," *IEEE Trans. Robot.*, vol. 38, no. 6, pp. 3807–3820, Dec. 2022.
[39] J.-Y. Kim and B.-H. Jun, "Design of six-legged walking robot, little crabster for underwater walking and operation," *Adv. Robot.*, vol. 28, no. 2, pp. 77–89, 2014.
[40] G. Picardi, A. Astolfi, D. Chatzievangelou, J. Aguzzi, and M. Calisti, "Underwater legged robotics: Review and perspectives," *Bioinspiration Biomimetics*, vol. 18, 2023, Art. no. 031001.
[41] G. Picardi, H. Hauser, C. Laschi, and M. Calisti, "Morphologically induced stability on an underwater legged robot with a deformable body," *Int. J. Robot. Res.*, vol. 40, no. 1, pp. 435–448, 2021.
[42] N. Plamondon and M. Nahon, "A trajectory tracking controller for an underwater hexapod vehicle," *Bioinspiration Biomimetics*, vol. 4, no. 3, 2009, Art. no. 036005.
[43] C. Georgiades, M. Nahon, and M. Buehler, "Simulation of an underwater hexapod robot," *Ocean Eng.*, vol. 36, no. 1, pp. 39–47, 2009.
[44] A. A. Shirgaonkar, O. M. Curet, N. A. Patankar, and M. A. MacIver, "The hydrodynamics of ribbon-fin propulsion during impulsive motion," *J. Exp. Biol.*, vol. 211, no. 21, pp. 3490–3503, 2008.
[45] Y.-h. Zhang, L.-b. Jia, S.-w. Zhang, J. Yang, and K. Low, "Computational research on modular undulating fin for biorobotic underwater propulsor," *J. Bionic Eng.*, vol. 4, no. 1, pp. 25–32, 2007.
[46] H. Liu and O. Curet, "Swimming performance of a bio-inspired robotic vessel with undulating fin propulsion," *Bioinspiration biomimetics*, vol. 13, no. 5, 2018, Art. no. 056006.
[47] F. Liu, K.-M. Lee, and C.-J. Yang, "Hydrodynamics of an undulating fin for a wave-like locomotion system design," *IEEE/ASME Trans. Mechatron.*, vol. 17, no. 3, pp. 554–562, Jun. 2012.
[48] J. Zou, J. Wang, and C. Ji, "The adhesive system and anisotropic shear force of Guizhou Gastromyzontidae," *Sci. Rep.*, vol. 6, no. 1, pp. 1–10, 2016.
[49] J. Wang, C. Ji, W. Wang, J. Zou, H. Yang, and M. Pan, "An adhesive locomotion model for the rock-climbing fish, Beaufortia kweichowensis," *Sci. Rep.*, vol. 9, no. 1, pp. 1–13, 2019.
[50] A. H. Jazwinski, *Stochastic Processes and Filtering Theory*. North Chelmsford, MA, USA: Courier Corporation, 2007.
[51] M. Mistry, J. Buchli, and S. Schaal, "Inverse dynamics control of floating base systems using orthogonal decomposition," in *Proc. IEEE Int. Conf. Robot. Autom.*, 2010, pp. 3406–3412.
[52] C. Gehring, S. Coros, M. Hutter, M. Bloesch, M. A. Hoepflinger, and R. Siegwart, "Control of dynamic gaits for a quadrupedal robot," in *Proc. IEEE Int. Conf. Robot. Automat.*, 2013, pp. 3287–3292.
[53] T. Fossen, "Guidance and control of ocean vehicles," Hoboken, NJ, USA: Wiley, 1994.
[54] J. Yu, M. Tan, J. Chen, and J. Zhang, "A survey on CPG-inspired control models and system implementation," *IEEE Trans. Neural Netw. Learn. Syst.*, vol. 25, no. 3, pp. 441–456, Mar. 2014.
[55] A. Badri-Spröwitz, A. A. Sarvestani, M. Sitti, and M. A. Daley, "BirdBot achieves energy-efficient gait with minimal control using avian-inspired leg clutching," *Sci. Robot.*, vol. 7, no. 64, 2022, Art. no. eabg4055.
[56] Q. Shi et al., "Development of a small-sized quadruped robotic rat capable of multimodal motions," *IEEE Trans. Robot.*, vol. 38, no. 5, pp. 3027–3043, Oct. 2022.
[57] F. Xie, Y. Zhong, R. Du, and Z. Li, "Central pattern generator (CPG) control of a biomimetic robot fish for multimodal swimming," *J. Bionic Eng.*, vol. 16, pp. 222–234, 2019.
[58] J. A. Acebrón, L. L. Bonilla, C. J. P. Vicente, F. Ritort, and R. Spigler, "The Kuramoto model: A simple paradigm for synchronization phenomena," *Rev. Modern Phys.*, vol. 77, no. 1, 2005, Art. no. 137.
[59] T. Kim, M.-j. Kim, and S.-C. Yu, "Neural network based CPG control method of undulating fin in underwater biomimetic robot," in *Proc. IEEE Underwater Technol.*, 2023, pp. 1–5.
[60] A. Dietrich, C. Ott, and A. Albu-Schäffer, "An overview of null space projections for redundant, torque-controlled robots," *Int. J. Robot. Res.*, vol. 34, no. 11, pp. 1385–1400, 2015.
[61] F. Flacco, A. De Luca, and O. Khatib, "Motion control of redundant robots under joint constraints: Saturation in the null space," in *Proc. IEEE Int. Conf. Robot. Autom.*, 2012, pp. 285–292.
[62] S. Garrido-Jurado, R. Muñoz-Salinas, F. J. Madrid-Cuevas, and M. J. Marín-Jiménez, "Automatic generation and detection of highly reliable fiducial markers under occlusion," *Pattern Recognit.*, vol. 47, no. 6, pp. 2280–2292, 2014.
[63] S. H. Maude and D. D. Williams, "Behavior of crayfish in water currents: Hydrodynamics of eight species with reference to their distribution patterns in southern ontario," *Can. J. Fisheries Aquatic Sci.*, vol. 40, no. 1, pp. 68–77, 1983.
[64] J. Ayers, "Underwater walking," *Arthropod Struct. Develop.*, vol. 33, no. 3, pp. 347–360, 2004.
[65] A. Crespi, K. Karakasiliotis, A. Guignard, and A. J. Ijspeert, "Salamandra robotica II: An amphibious robot to study salamander-like swimming and walking gaits," *IEEE Trans. Robot.*, vol. 29, no. 2, pp. 308–320, Apr. 2013.
[66] H. Kang, H. Shim, B.-H. Jun, and P.-M. Lee, "Development of a specialized underwater leg convertible to a manipulator for the seabed walking robot CR200," *J. Inst. Control, Robot. Syst.*, vol. 19, no. 8, pp. 709–717, 2013.
[67] H. Komura, S. Kitano, H. Yamada, and G. Endo, "Gliding, swimming and walking: Development of multi-functional underwater robot glide walker," in *Proc. IEEE Int. Conf. Robot. Autom.*, 2014, pp. 2944–2949.

Taesik Kim received the B.E. degree in mechanical engineering from the Ulsan National Institute of Science and Technology (UNIST), Ulsan, South Korea, in 2018. He is currently working toward the Ph.D. degree with the Department of Convergence IT Engineering, Pohang University of Science and Technology (POSTECH), Pohang, South Korea.

His research interests include field robotics, bioinspired soft robotics, and challenging robot system.

Juhwan Kim received the B.E. degree from the Department of Electrical Engineering and the Ph.D. degree from the Department of Convergence IT Engineering, Pohang University of Science and Technology, Pohang, South Korea, in 2015 and 2023, respectively.

Since 2023, he has been a Staff Engineer with the Robot Center, Samsung Research, Samsung Electronics, Seoul, South Korea.

Son-Cheol Yu (Member, IEEE) received the M.E. and Ph.D. degrees from the Department of Ocean and Environmental Engineering, University of Tokyo, Tokyo, Japan, in 2000 and 2003, respectively.

He is currently a Professor with Department of Convergence IT Engineering, Electrical Engineering and Division of Advanced Nuclear Engineering, Pohang University of Science and Technology, Pohang, South Korea.

Authorized licensed use limited to: POSTECH Library. Downloaded on August 30,2024 at 11:15:24 UTC from IEEE Xplore. Restrictions apply.